Kineto-static analysis of a hybrid manipulator consisting of rigid and flexible limbs with locking function for planar shape morphing☆

Yinjun Zhao[1], Fengfeng Xi[3], Guangbo Hao[4], Yingzhong Tian[2], Long Li[2], Jieyu Wang[2]*
[1]School of Mechanical Engineering, University of Shanghai for Science and Technology, Shanghai 200093, China
[2]School of Mechatronic Engineering and Automation, Shanghai Key Laboratory of Intelligent Manufacturing and Robotics, Shanghai University, Shanghai 200444, China
[3]Department of Aerospace Engineering, Toronto Metropolitan University, Toronto ON M5B 2K3, Canada
[4]School of Engineering and Architecture-Electrical and Electronic Engineering, University College Cork, Cork, Ireland
*Corresponding author: jywang2021@shu.edu.cn

Abstract — The incorporation of lockable passive backbones into active compliant morphing systems efficiently results in lightweight, high-load, and large deformation systems. However, there exist challenges in kineto-static analysis due to the interaction between rigid reconfigurable kinematic constraints and the nonlinear deformation of actuated flexible limbs. This paper addresses these issues by developing a kineto-static method to analyze the motion in a novel planar 3-DOF shape-morphing manipulator. The manipulator features two actuated flexible limbs with a lockable variable geometry truss (LVGT). In this study, two isostatic topologies are selected for reconfigurable motion control under external tip loads. A multi-step sequential control strategy is proposed to maneuver the manipulator's platform for desired poses. Then, a constrained-trajectory-based kinematic model is proposed for an inverse kinematic solution considering motion planning. Subsequently, a kineto-static model is introduced, considering constraints from rigid and flexible limbs, aiming to distribute distributing redundant actuation forces. Finally, nonlinear finite element analysis (FEA) and experiments are carried out to validate the effectiveness of the proposed method.

Keywords—Rigid-flexible reconfigurable parallel manipulator, Shape morphing structure, Kinematics, Kineto-static analysis, Sequential motion control

1. Introduction

Shape-morphing manipulators [1, 2] have remarkable abilities to adapt, evolve or change their shapes, properties or behaviors in response to environmental changes. Their potential applications span a broad spectrum, ranging from the macro-scale to the micro-scale, encompassing fields such as civil engineering and architectures [3-5], space/aerospace [6-12], bionic continuum/soft robots [13-18], minimally invasive surgery systems [19-21], and micro-electro-mechanical systems [22-24]. However, designing large-scale morphing structures for space or aerospace morphing systems remains a significant challenge and an open issue [1, 25, 26]. The development of them necessitates a delicate balance of conflicting requirements, including a compact structure, lightweight design, high load-carrying capacity, as well as multi-DOF and continuum large-scale deformability.

It is widely acknowledged that conventional rigid-body mechanisms [7, 27-30] suffer from significant weight penalties and require bulky actuation systems to achieve multi-DOF, continuum, and large-scale shape morphing. As a result, compliant mechanisms are likely to serve as the basis for developing such a morphing system in the future [31-33]. However, compliant systems designed for large-scale morphing currently lack load-carrying ability and stiffness. In addition, the nonlinear deformation of the flexible members [9, 34, 35] poses considerable challenges for motion analysis and pose control. This kind of design can be seen in Fig. 1(a), a parallel continuum mechanism (PCM) consisting of two actuated flexible limbs with no internal backbones.

Despite the utilization of variable stiffness technology [36-41] and employing fixed-length flexible backbones [42, 43] (illustrated in Fig. 1(b), a primary flexible backbone is added in a PCM, capable of withstanding some loads and deforming within specified limits) to improve the load-carrying abilities, these approaches fall short in addressing high-load scenarios. Instead, a

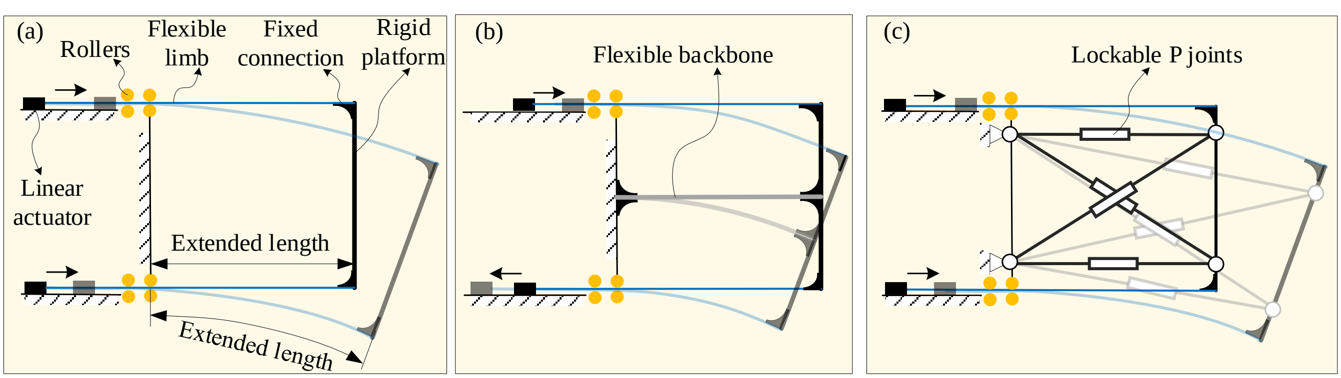

Fig. 1. A parallel continuum morphing system with (a) no backbone, (b) a compliant backbone, and (c) a rigid LVGT backbone.

☆ This paper in-part has been accepted for presentation at IFToMM CCMMS 2024 Conference, Tianjin, China. Acronyms used in this paper are explained in Appendix E.

simple and effective alternative is to use a LVGT backbone constructed with multiple lockable P joints [44-47] as the main load-bearing structure of the morphing system (Fig. 1(c)), which was proposed in our previous study [48-50]. However, the design incorporating both actuated flexible limbs and passive lockable limbs introduces new challenges in kinematics and static analysis, which differ from those posed by existing PCMs and rigid parallel mechanisms (PMs).

Figure 2 shows the structure design of the 3-DOF manipulator we proposed (Figs. 2(a)-(c)) and one of its potential applications in morphing airfoil wings (Figs. 2(d)(e)). It can be seen as a passive LVGT covered by an active PCM. The LVGT consists of multiple units I and II, which have different limb orientations on the diagonal (Fig. 2(b)). In order to maintain the shape of the manipulator without energy consumption, the P joints are designed as a normal locking form. In our previous studies, we proposed to use spring ratchet mechanisms and single acting pneumatic cylinders to design the P joint [44]. We used this lockable P joint design for constructing the prototype in this paper shown in Fig. 2(d). Besides, in order to further reduce the dimension, weight, and complexity of the lockable P joint, as well as to achieve continuum locking positions, we recently proposed to use compliant mechanisms (CM) integrated with smart materials (piezoelectric stack and SMA actuations) to design the lockable P joint [45] [51]. In addition, Moosavian et. al proposed a hydraulic-cylinders-and-valves based lockable joint [46], which can also be used to construct the LVGT. One can refer to these existing studies to choose a suitable lockable joint for a specific application.

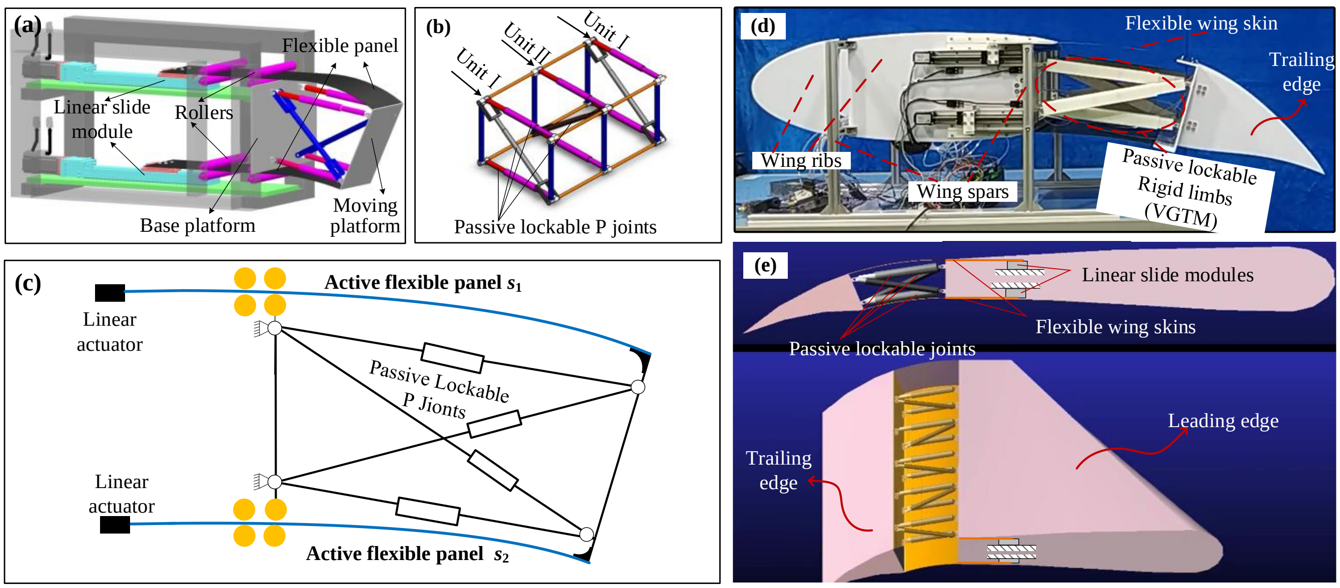

Fig. 2. The structure design of (a) the proposed shape-morphing manipulator, (b) its internal LVGT, and (c) its simplified planar structure for kineto-static analysis. The manipulator has the potential application in morphing airfoil wings, as the prototype in (d), and the CAD model in (e). In the morphing wing application, the LVGT is assembled in the wing box. Linear actuators are assembled on wing ribs, actuating flexible wing skins, and the trailing edge is assembled on the moving platform.

For the potential morphing wing applications, the LVGT could assembled in the wing box to withstand loads and linear actuators can be assembled on wing ribs to actuate the flexible wing skins (Fig. 2(d)). By releasing lockable joints at specific positions and driving the flexible skins, the airfoil shape can be changed. Note that, in practical applications, it is not possible to guarantee consistency in state switching across all lockable joints. Hence, when switching motion topologies, we lock all P joints first and then release the desired joints, to avoid unnecessary motion topologies.

While pioneers have made significant progress in understanding the motion and statics of parallel manipulators with multiple rigid limbs [52-57] or flexible limbs [13, 37, 38, 58-63], our hybrid manipulator, which features both actuated flexible limbs and passive lockable limbs, presents new challenges in kineto-statics analysis. The main differences in kineto-statics analysis of this manipulator from the other PMs/PCMs are listed below:

1）*The constrained motion topologies from the LVGT can be reconfigured*: By releasing specific lockable joints, the LVGT can obtain different motion topologies and load-carrying abilities. We can choose appropriate motion topologies to adjust the manipulator's pose. Besides, the kinematics that includes motion topology reconfiguration is also worth studying, as we can use the combination of some reduced DOF motion topologies to achieve full mobility control of the manipulator.

2）*The number of constrained DOF and actuated DOF may vary, resulting in redundant actuation of flexible limbs*: Various actuation modes can be achieved due to the reconfigurability of the LVGT. If the actuated DOFs are equal to the LVGT's DOFs, the manipulator is fully actuated. If the actuated DOFs exceed the LVGT's DOFs, the manipulator becomes redundantly actuated. In redundant actuation modes, the extra actuated flexible limbs provide additional driving forces, resulting in a variety of actuation force distributions for achieving a desired pose of the moving platform, with different shapes of flexible limbs. This means that there will be an infinite number of inverse kineto-statics solutions for the redundant driven cases.

Hence, the manipulator's motion is determined by the kinematic constraints imposed by the rigid limbs, the coupled nonlinear deformation of the flexible limbs and the actuation modes of the PCM. Given this complex motion principle, a kineto-static model is essential for describing the manipulator's motion, which can be further employed in simulation-based design optimization and open-loop pose control.

This study can also be seen as a supplementary and contribution to the research domain of kinematics and kinetostatic analysis in PCMs, since fundamentally the motion of the manipulator is realized in-part by coupled deformation of flexible limbs. Nevertheless, the distinctive structural and motion characteristics of our proposed manipulator preclude the direct utilization of existing methods.

For PCMs, the kinematics problem is very complicated since the motion of the manipulator is related to the coupled non-linear deformation of flexible limbs [37, 38, 58-63]. This complexity arises from the representation of flexible limb deformation using sets of differential equations [34, 64, 65], namely geometric nonlinearity during large deformation. As for the forward kinematics problem (FKP) of PCMs, Wang *et al* used the large deformation Euler-Bernoulli beam theory with Elliptic integral solutions to model the flexible beam in a planar PCM [61]. They solved the FKP using an optimization model with the objective of achieving static balance for the moving platform. Ma and Chen explored the FKP of planar PCMs under no tip loads using the chained beam constraint model (CBCM) [62].

As for the inverse kinematics problem (IKP) of the PCMs, it becomes more complex since a desired configuration may not in a stable state, i.e., the configuration may not reach since the total potential energy of the compliant system is not locally minimized. Rucker *et al* proposed a spatial PCM constructed with multiple flexible limbs [60] and established its inverse kineto-static model using the Cosserat rod model [59, 60]. They solved the IKP of such manipulators by finding the boundary values of a differential equation system. Besides, they also investigated the efficient numerical solution of this kineto-static model [66] and the elastic stability problem in IKP [67]. It's worth noting that, due to the presence of rigid constraints from the LVGT in our proposed design, we do not encounter this issue in the IKP. Chen *et al* proposed a discretization-based method [68] for modeling the nonlinear large deformation of flexible limbs in spatial PCMs for solving the FKP and IKP of PCMs [68, 69]. This method approximates the PCM as a hyper-redundant rigid link system, using Lie group formulations for kineto-static analysis rather than the continuum mechanics of elastic materials.

In addition, as for the kinematics of manipulators consisting of rigid and flexible limbs, most researches focused on manipulators constructed by serial mechanisms with cable driven [70]. The deformation of cables is linear under tension force, and the rigid constraints of such manipulators could be constructed using commonly used Denavit-Hartenberg methods, which are different from the studied kinetostatic problem involving coupled nonlinear deformation and variable rigid constraints from the LVGTs.

In our previous work [48], we initially investigated the kinematics of the morphing manipulator with an LVGT backbone. The previous method was based on geometric analysis, requiring manual analysis to determine the number of motion steps and artificial observation of the LVGT's geometry to avoid singularity positions. It's also worth noting that the previous kinematics model was only based on constraints from the rigid part of the manipulator, without considering the impact of the actuated flexible limbs. As a result, the previous model couldn't comprehensively elucidate or predict the manipulator's motion based on its real working principle. Furthermore, the actuation forces and actuation distances of the flexible limbs could not be predetermined.

In this study, we develop an improved modeling method for multi-step motion with topology reconfiguration of the LVGT. This approach is based on the center trajectory of the moving platform to address the problem mentioned above. It provides a simple way to mathematically describe the coupled relationship of multi-step motion, allowing for easy determination of the number moving steps, potential moving paths, the optimal moving trajectory, and workspace while considering singularity.

Additionally, we introduce a framework for solving the inverse kineto-static problem of the manipulator in redundant actuation modes. This framework is founded on the manipulator's fundamental motion principles. The proposed kineto-static model considers constraints from the rigid moving pair, deformation equation constraints from the flexible limbs, as well as the coupling effects of PCM and LVGT (i.e., the actuation modes of the PCM and constrained topologies of the LVGT). This results in a more comprehensive grasp of the manipulator's motion, allowing for precise predictions of the actuation forces and distances of the flexible limbs.

The proposed model could be used to maneuver the manipulator to realize large-scale shape morphing, with the consideration of the constraints from rigid and flexible limbs as well as optimize the actuation forces distribution. Besides, the model could also be used in the simulation-based structure optimization of the manipulator.

In general, the technical study and main contributions of this article are concluded as follows:

1) A trajectory-constraint-based kinematic model is proposed to solve the multi-step forward kinematics, workspace analysis as well as the inverse kinematics with motion planning.
2) Development of a framework to establish the kineto-static model for the proposed manipulator, considering various LVGT constrained modes and PCM actuation modes.
3) Intensive studies are conducted on redundant actuation modes, including the creation of an inverse kineto-statics model that considers the distribution of redundant actuation forces, the investigation of motion and driving force characteristics through case studies, and the examination of the influence of LVGT dimensions on the actuation distance and forces of flexible limbs.
4) Experiments and nonlinear FEA were conducted to verify the effectiveness and accuracy of the proposed models.

The remainder of this paper is organized as follows. Section 2 re-visits the reconfigurable motion topologies of the manipulator from the perspectives of mechanism and truss structure design, respectively. Additionally, this section discusses the singularity of the selected topologies which could withstand relative high loads during shape morphing. In Section 3, we propose a constrained-trajectory-based kinematic model to address the multi-step coupled kinematics problem. In Section 4, we present the kineto-static model, which is employed to determine the internal force distribution on each limb when subjected to external tip loads. Section 5 describes the FEA and experiments carried out to verify the modeling approach. Finally, we provide our conclusions in the last section.

2. Re-visiting motion topologies

This section focuses on the analysis of the reconfigurable topologies of the manipulator. There are 4 variable length rigid limbs in the LVGT (L_1, L_2, L_3, L_4), in which L_1 is the upper limb, L_4 is the bottom limb, L_2 is right tilt diagonal limb, and L_3 is left tilt diagonal limb, as shown in Fig. 3(a). By locking different P joints, motion topologies can be reconfigured. These motion topologies exhibit varying kinematic properties and load-carrying capacities. We re-visit the motion topologies of the mechanism in this section from the perspective of mechanism design and truss structure design respectively, to help the reader better understand the basic characteristics of this manipulator. Besides, we select topologies that are capable of movement and also featured a fixed, statically determinate structure, enabling the manipulator to withstand loads during motion. At last, we introduce the singularity positions of the manipulator.

2.1. Mobility and stability analysis of the manipulator

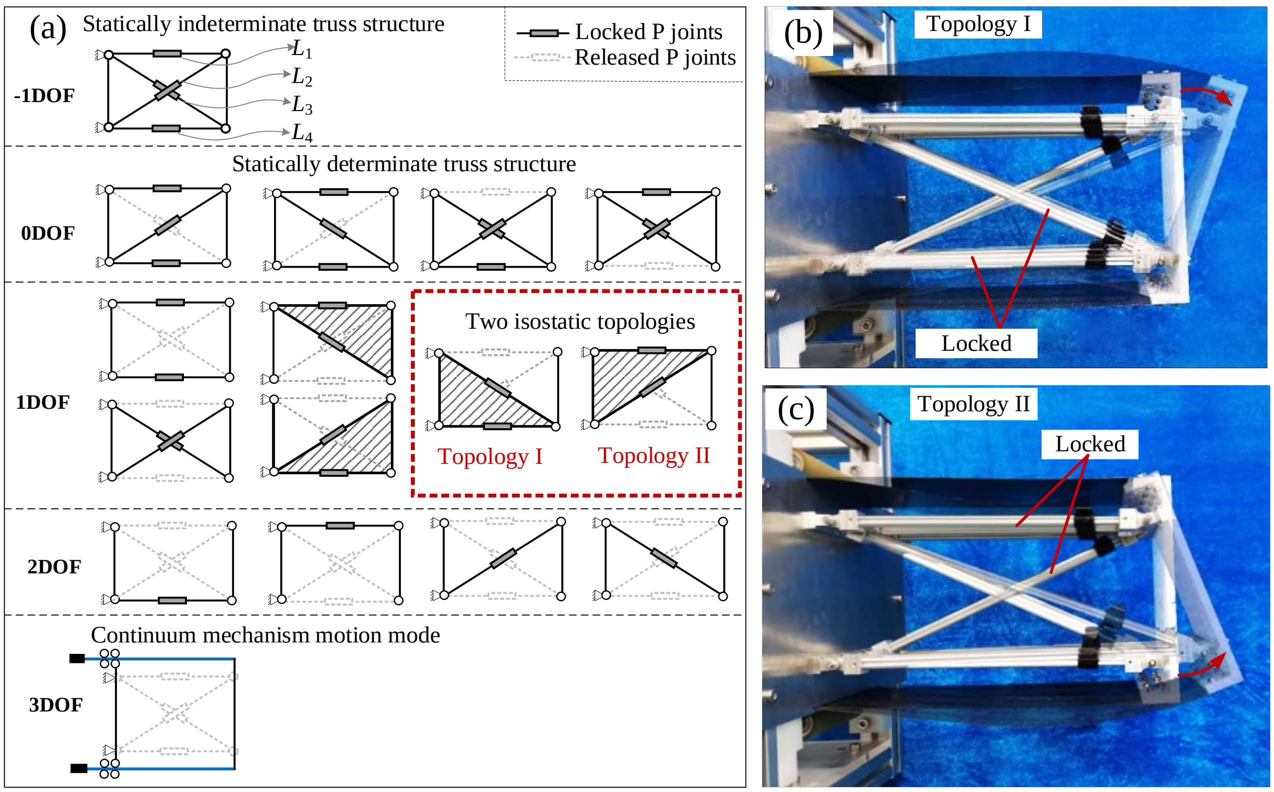

Fig. 3. Motion topology analysis of the manipulator. (a) shows the different topologies and mobilities that could be obtained through locking different P joints. There are two special cases called isostatic topologies I and II (in the red dotted box) could be obtained, which have fixed trusses to withstand loads and have 1 DOF for motion. (b) shows the moving process of Topology I operated on a prototype. (c) The moving process of Topology II operated on a prototype.

Figure 3(a) lists the reconfigured topologies of the manipulator, showing that the manipulator can realize the topology reconfiguration among truss structures, rigid-flexible mechanisms, and continuum mechanisms. If no P joint is released, the manipulator turns to a statically indeterminate (hyper-static) truss with a static indeterminacy of 1. If 1 P joint is released, the manipulator turns to a statically determinate truss. If 2 or 3 P joints are released, 1-DOF or 2-DOF motion topologies could be obtained, respectively. If all the 4 P joints are released, without any constraints from rigid limbs, the manipulator could obtain the 3-DOF continuum mechanism motion mode. The detailed methods for analyzing the mobility and stability of the manipulator are given in Appendix A.

The truss structures exhibit excellent load-carrying capacity in comparison to the rigid-flexible mechanisms and continuum mechanisms. However, our goal is to develop a manipulator can withstand desired loads not only in a stationary state but also during motion. After considering all topologies with 1 and 2 DOFs, only two isostatic topologies I or II (Fig. 3(b) and (c)) could meet our requirements. These two topologies incorporate fixed triangular trusses in the structure, serving as a stable backbone for the manipulator. In Topology I, the triangular support is constructed by the bottom limb L_4, the left tilt diagonal limb L_3 and the fixed base, whereas in Topology II, the triangular support is constructed by the upper limb L_1, the right tilt diagonal limb L_2, and the fixed base. Although these isostatic stable topologies only have 1 DOF, the 3 DOFs of the moving platform can be fully controlled through topology switching and multi-step motion (to be discussed in Sec. 3).

2.2. Singularity positions

For Topologies I and II, the singularity at the extreme displacement can be easily observed in Fig. 4. For Topology I, the singularity occurs when the moving platform BD is parallel with the bottom limb L_4, where B and D denote the endpoints on both sides of the moving platform. For topology II, the singularity occurs when BD is parallel with the upper limb L_1 (BD//L_1). The blue lines in Fig. 4 represent the intermediate state of the LVGT during motion. Due to the singularity, the chosen topologies yield limited workspace. More specifically, even if not considering the influence of flexible limbs, the displacement of the midpoint of

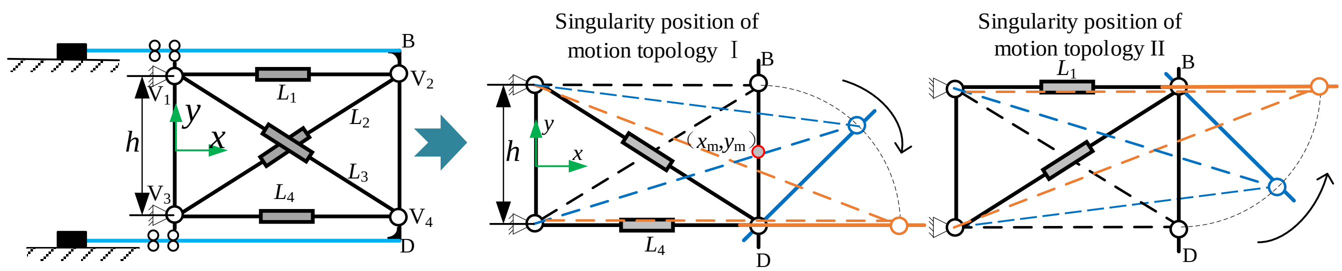

Fig. 4. Singularity positions of the manipulator (yellow lines). The singularity occurs when the moving platform is parallel with L_4 (BD//L_4) for topology I and when the moving platform is parallel with L_1 (BD//L_1) for topology II, described as yellow lines in this figure. The blue lines represent the intermediate state of the LVGT during motion.

the moving platform x_m, y_m are all less than $h/2$, where h is the distance between two R joints V_2 and V_4 in LVGT, as labeled in Fig.4. Hence, if the design space has a limitation on h, the manipulator can only produce very small displacements in both x and y directions. However, through motion topology switching and multi-step motion, this problem could be addressed including enlarging workspace, avoiding extreme displacement singularity, and realizing 3-DOF pose control.

3. Constrained-trajectory-based multi-step kinematic model and motion planning

This section aims to establish the kinematic model considering the topology reconfiguration of the LVGT. As illustrated in Fig. 5, the moving process contains motion topology switch between topologies I and II. Hence, a mathematical mapping (represented as f_g in Fig. 6) needs to be established to connect the pose of the moving platform (x_m, y_m, θ) with the number of motion steps (n) and the corresponding intermediate states of the moving platform. In this section, we introduce a constrained-trajectory-based kinematic model to address this problem. Note that since the entire motion process involves different motion topologies switching, the controllable DOFs cannot be obtained directly by using the formula for calculating DOFs. It is necessary to combine with the motion analysis proposed in this section to obtain them. We will also give a detail explanation for why we can use these two 1-DOF motion topologies to achieve the full mobility control.

In the next section, we will present the inverse kineto-static model for each motion step, which describing the relationship between the task space (the pose of the moving platform) and constraint space (L_1^i, L_2^i, L_3^i, L_4^i) as well as the actuation space (s_1^i, s_2^i), denoted as the mappings f_1^i and f_2^i in Fig. 6.

3.1. Constrained-trajectory-based kinematic model

Referring to Fig. 5, the position and orientation of the moving platform can be adjusted by alternating between motion topologies I and II. As a result, the center of the manipulator will follow a multiple-tangent-arcs, as illustrated in Fig. 7. Such a trajectory could be described by the parameters including the number of arc segments n, the center angle of each arc (${}^0\theta_1$, ${}^1\theta_2$, ${}^2\theta_3\ldots{}^{n-1}\theta_n$) and their radius $h/2$. For an n-step motion, local coordinate systems representing the pose of the moving platform in each step motion are placed at the center of the moving platform. The global coordinate system $\{\boldsymbol{x}_\mathbf{B}, \boldsymbol{y}_\mathbf{B}\}$ is fixed at the center of the base platform.

Referring to Fig. 7, supposing that the manipulator begins with Topology II and counter-clockwise rotation is positive, the final pose (orientation ${}^{\mathrm{B}}\theta_n$ and position ${}^{\mathrm{B}}\mathbf{P}_n$) of the end platform in global coordinates after multi-step motion can be calculated as (If the motion begins with topology I, just replace all the $(-1)^{i-1}$ and $(-1)^{j-1}$ by $(-1)^{i}$ and $(-1)^{j}$ in Eqs. (1) and (2) respectively.)

$$\begin{cases} {}^{\mathrm{B}}\theta_n = \sum_{i=1}^{n} (-1)^{i-1}\, {}^{i-1}\theta_i \\ {}^{\mathrm{B}}\mathbf{P}_n = {}^{\mathrm{B}}\mathbf{P}_0 + \sum_{i=1}^{n} \left(\prod_{j=1}^{i} {}^{j-1}\mathbf{R}_j \right) {}^{i-1}\mathbf{P}_i \end{cases}, \tag{1}$$

where ${}^{j-1}\mathbf{R}_j$ denotes the rotation matrix from coordinates $\{\boldsymbol{x}_j, \boldsymbol{y}_j\}$ to $\{\boldsymbol{x}_{j-1}, \boldsymbol{y}_{j-1}\}$, ${}^{i-1}\mathbf{P}_i$ stands for the translation vector from coordinates $\{\boldsymbol{x}_i, \boldsymbol{y}_i\}$ to $\{\boldsymbol{x}_{i-1}, \boldsymbol{y}_{i-1}\}$, and ${}^{\mathrm{B}}\mathbf{P}_0$ stands for the position vector of point $\mathbf{O}_0$ with respect to the origin $\{\boldsymbol{x}_\mathbf{B}, \boldsymbol{y}_\mathbf{B}\}$. They can be expressed as

$${}^{j-1}\mathbf{R}_j = \begin{bmatrix} \cos\left[(-1)^{j-1}\, {}^{j-1}\theta_j\right] & -\sin\left[(-1)^{j-1}\, {}^{j-1}\theta_j\right] \\ \sin\left[(-1)^{j-1}\, {}^{j-1}\theta_j\right] & \cos\left[(-1)^{j-1}\, {}^{j-1}\theta_j\right] \end{bmatrix} \in SO(2), \tag{2}$$

$$
{}^{i-1}\mathbf{P}_i = (-1)^{i-1}\left[\frac{h}{2}\sin(-1)^{i-1}\,{}^{i-1}\theta_i \quad \frac{h}{2}-\frac{h}{2}\cos(-1)^{i-1}\,{}^{i-1}\theta_i\right]^{\mathrm{T}} \in \mathbb{R}^2,
$$

$$
{}^{\mathrm{B}}\mathbf{P}_0 = \left[L_0 \quad 0\right]^{\mathrm{T}} \in \mathbb{R}^2.
$$

where L_0 stands for the distance between coordinate system $\{\boldsymbol{x}_\mathbf{B}, \boldsymbol{y}_\mathbf{B}\}$ and $\{\boldsymbol{x}_\mathbf{0}, \boldsymbol{y}_\mathbf{0}\}$ in x direction. Besides, the homogeneous transformation matrix ${}^{\mathrm{B}}\mathbf{T}_i$ from the base coordinate system $\{\boldsymbol{x}_\mathbf{B}, \boldsymbol{y}_\mathbf{B}\}$ to the local coordinate systems $\{\boldsymbol{x}_i, \boldsymbol{y}_i\}$ can be obtained as

$$
{}^{\mathrm{B}}\mathbf{T}_i = \begin{bmatrix} \mathbf{R}_z({}^{\mathrm{B}}\theta_i) & {}^{\mathrm{B}}\mathbf{P}_i \\ 0 & 1 \end{bmatrix} \in SE(2). \tag{3}
$$

When $i=n$, the final pose can be obtained.

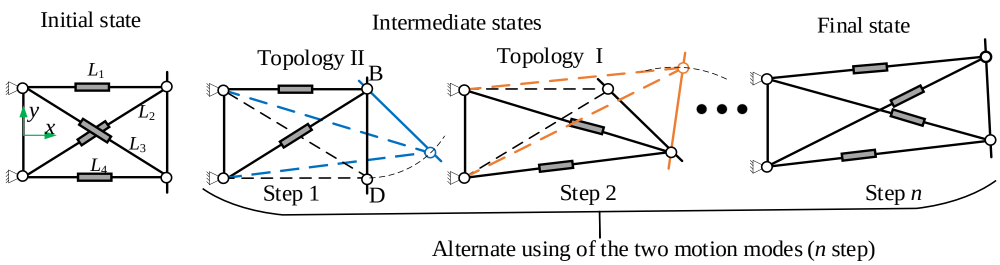

Fig. 5. The moving process of the manipulator, which contains motion topology switching the 1-DOF topology II and I, aiming for full mobility control of the moving platform as well as withstanding external loads during motion. The motion process given in this figure starts from topology II, while also could starts from topology I.

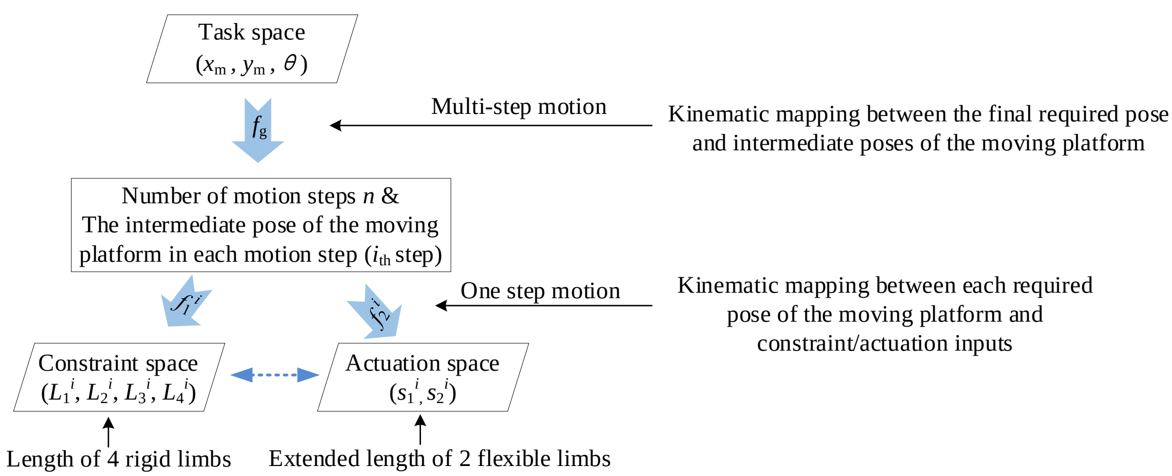

Fig. 6. Inverse kinetostatic mapping relationships. There are three mappings. The first mapping denoted as f_g is the relationship between the pose of the moving platform (x_m, y_m, θ) and the number of motion steps n and the corresponding intermediate poses of the moving platform. For each step motion, two mathematic mappings described as f_1^i and f_2^i exist, where f_1^i represents the relationships between task space (the pose of the moving platform) and constraint space (L_1^i, L_2^i, L_3^i, L_4^i), and f_2^i represents the relationships between the task space and the actuation space (s_1^i, s_2^i).

Till now, the forward kinematic model of the multi-step motion is established. By analyzing the kinematic model expressed by Eq. (1), we can find this is a nonlinear equations system consisting of 3 equations (reflecting the position and orientation of the end platform) with n+1 unknown parameters including (n, ${}^0\theta_1$, ${}^1\theta_2$, ${}^2\theta_3 \ldots {}^{n-1}\theta_n$). In theory, given the angles of the arcs in each step motion, the final pose of the moving platform can be solved (FKP). In turn, given the final position and orientation of the moving platform, the above equations can be used to determine the number of motion steps and the poses of each step (IKP).

However, the inverse kinematic solutions may not be unique, or may not have the reachability of the desired pose, mainly depending on the number of motion steps. Let us observe the moving path in Fig. 7 again, it could be seen as an equivalent nR planar serial mechanism. Hence, if we want to control the 3 DOF of the moving platform, n should take a minimum value of 3, *i.e.*, at least 3 steps of motion are required for a 3-DOF shape morphing control. In Appendix B, we also give the analytical inverse kinematic solution for the 3-step motion case. When n>3, the equivalent nR serial mechanism has redundant DOFs, so the inverse kinematic model will have countless solutions and numerical methods could be used to solve the inverse kinematics. Increasing the number of steps n expands the workspace but will have multiple inverse kinematic solutions.

In practical applications, one can further examine these intermediate motion states to figure out whether they have any negative impact on system's performance. Moreover, given the non-uniqueness of inverse kinematic solutions, there is a room for further optimizing the motion trajectories to mitigate this issue. For instance, in the application of morphing wings, the motion path can be optimized by studying how the motion process influences the aircraft's center of lift and center of gravity. In fact, the primary potential application scenarios of the manipulator should focus on instances where the achieved deformation shape is of paramount concern as required in morphing wings, morphing antennas and morphing buildings; while the intermediate shapes during the deformation process are not stringent concerned.

In this paper, when encounter the problem of multiple solutions, we select the minimal number of steps n with the shortest trajectory to ensure a concise and efficient movement process.

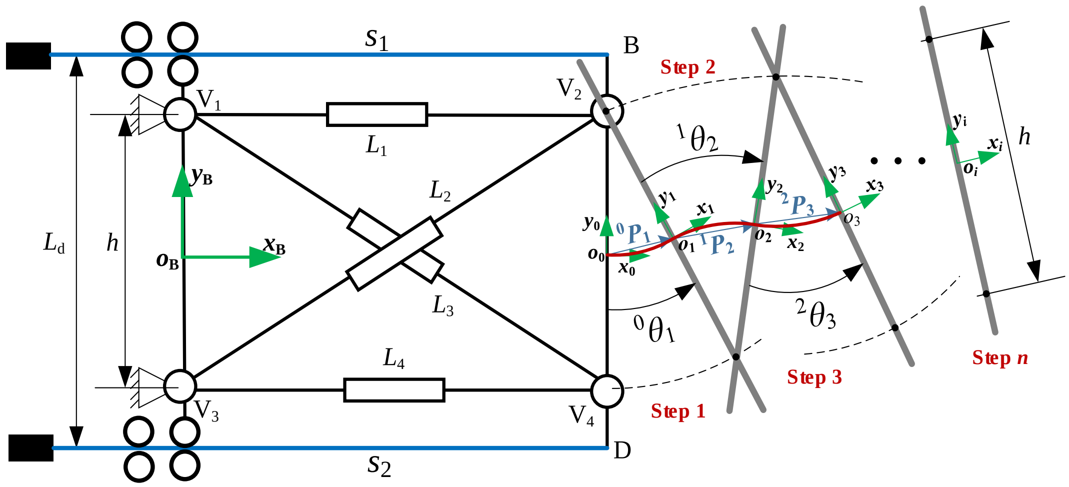

Fig. 7. The center trajectory constraints (red curve) of the moving platform for n-step motion. The intermediate poses of the moving platform during the multi-step motion process. When the manipulator is in mode II or I, the end platform rotates around V_2 or V_4. Hence, the moving path of the center of the moving platform is a multiple-tangent-arcs.

3.2. The optimal inverse kinematic solution with motion planning

For a desired pose that needs more than 3 steps to reach, multiple trajectories exist. We select the shortest trajectory. Referring to the multi-segment tangent arcs trajectory shown in Fig. 7, the length of the n steps trajectory L_t can be calculated as

$$L_t = \frac{h}{2}\sum_{i=1}^{n} {}^{i}\theta_{i-1} \ . \tag{4}$$

Then, in order to obtain the inverse kinematics solution of the shortest path, we could use the following optimization model:

$$\boldsymbol{\theta}^* = \underset{\left\{{}^{i-1}\theta_i\right\}_{i=1,\cdots,n}}{\arg\min} \frac{h}{2}\sum_{i=1}^{n} {}^{i-1}\theta_i \tag{5a}$$

$$\textbf{S.t.} \begin{cases} \text{Eq (1)}, & \text{Trajectory constraints} \\ L_z \le L_{\max},\ z = 1,2,3,4, & \text{Length constraints of rigid limbs} \\ \left|{}^{\mathrm{B}}\theta_i\right| = \left|\sum_{j=1}^{i} (-1)^{j-1}\ {}^{j-1}\theta_j\right| \le \theta_{\max},\ i = 1,2,\ldots n, & \text{Constraints from flexible limbs} \end{cases} \ . \tag{5b}$$

The constraints in the optimization model are from two aspects. One is the constraints from the internal passive lockable LVGT, including trajectory and rigid limb length constraints. The other constraints come from flexible limbs. Excessive bending of flexible panels may result in motion interference between flexible limbs and rigid limbs, or the internal forces exceed the strength of flexible panels or the strength of the soft-panel-to-end-platform connection. These kinds of constraints are approximately expressed by the limitation of the deflection angle of the end platform in each moving step ($\theta_{\max}$) under the assumption that the end platform is perpendicular to the flexible panels.

For solving the inverse kinematic model, Eq. (1) can firstly be used to try a 3-step motion. If there is no solution, then Eq. (5) can be used to try for more step motion until the solution could be found. Alternatively, we can use the workspace of different step motions to preliminary judge the minimal moving steps. By solving the inverse kinematic model, parameters (${}^{0}\theta_1$, ${}^{1}\theta_2$, ${}^{2}\theta_3$... ${}^{n-1}\theta_n$) could be obtained and then the pose of each intermediate pose can also be obtained by Eq. (3).

Although the constraints from the flexible limbs could be precisely expressed by the governing equations of the flexible limbs (as detailed in the later Sec. 4), this will significantly increase the complexity of the calculation due to the geometry nonlinearity of the large deformation members. Besides, if the governing equations are used, any other factors that affect the deformation of the flexible members should be included in the motion constraints, such as the actuation mode of the PCM, constrained mode of the LVGT, and external loadings. These factors will further lead to overly complex mathematical models. Therefore, the kinematic model presented in this section offers a more straightforward approach to achieve precise 3-DOF pose control.

3.3. Workspace analysis for multi-step motion

Equation. (5b) can be used to simulate the workspace under different steps. Specifically, Eq. (1) serves as the function for plotting the workspace, and the remaining equations in Eq. (5b) serve as constraint equations to produce data inputs of (${}^{0}\theta_1$, ${}^{1}\theta_2$, ${}^{2}\theta_3 \ldots {}^{n-1}\theta_n$) for Eq. (1). The reachable positional workspace of the prototype described in Sec. 5 are shown in Fig. 8, including the cases for 3, 4 and 5 steps motion. Here we set $\theta_{\max} = \pi/6$, h=130mm and set no limit on $L_{\max}$ to better show the potential largest workspace for multi-step motion. The blue region is the positional workspace for the 3-step motion, the red region is for the 4-step motion, and the yellow region is for the 5-step motion.

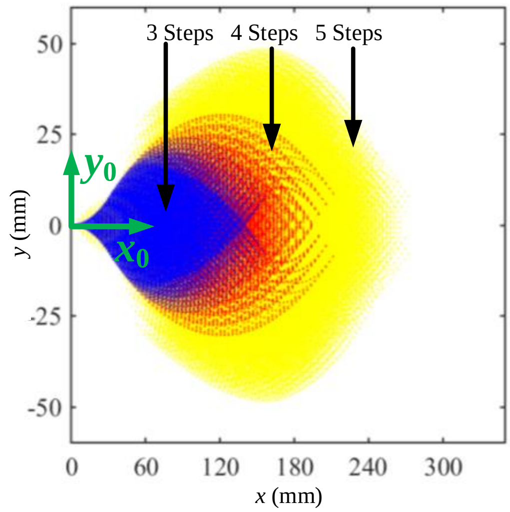

Fig. 8. Positional workspace for different numbers of motion steps. Here we set $\theta_{\max} = \pi/6$, h=130mm and set no limit on $L_{\max}$ to better show the potential largest workspace for multi-step motion.

4. Kineto-statics analysis of the manipulator

The above section addressed the IKP related to multi-step kinematics to determine the required number of steps and each intermediate state necessary to achieve the final desired pose. In this section, from the perspective of the actual motion principle, we give a framework to conduct the kineto-static analysis for each one-step motion of the manipulator, *i.e.*, establishing the mapping f_2: $\{x_{\mathrm{m}}, y_{\mathrm{m}}, \theta\} \rightarrow \{s_1, s_2\}$, as shown in Fig. 9(a). Besides, by solving the kineto-static model, the overall static force state of the mechanism could also be obtained.

To establish the model, we need to consider three types of constraints, as illustrated in Fig. 9(b) (c) and (d):

1) The governing equations of large deformation flexible limbs (Fig. 9(b)): The chained-beam-constrained-model (CBCM) [71] is used in this paper, which could be described as f_4: $\{P_0, F_0, M_0, s\} \rightarrow \{X_0, Y_0, \theta_0\}$, where P_0, F_0, M_0 are load parameters, X_o, Y_0, θ_0 are deflection parameters, and s is the length of the beam. The modeling process for this part will be introduced in Sec. 4.1.

2) The structural balance of the manipulator (Fig. 9(c)): The structural balance of the manipulator is reflected by the static balance of the moving platform. which could be written as $\mathbf{J} \times \mathbf{f}_{\mathrm{Internal}} = -\mathbf{f}_{\mathrm{External}}$, where $\mathbf{J}$ is the statics Jacobian matrix, $\mathbf{f}_{\mathrm{Internal}}$ is the vector of scalar internal forces and moments from the LVGT and the PCM, $\mathbf{f}_{\mathrm{External}}$ is the vector of the scalar external forces and moments exerted on the moving platform. This part will be introduced in Sec. 4.2.

3) The actuation modes of the PCM and constrained topologies of the LVGT (Fig. 9(d)): For this manipulator, only one flexible limb is sufficient for motion control since each step motion is 1-DOF. However, double actuation will offer more driven forces and better transmission efficiency of the driving forces in different motion topologies. Referring to Fig. 9(d.1), the bottom flexible limb is actuated, which allows full mobility control of topology I. However, the transmission efficiency of the driving forces is very low, due to the short force arm. To improve the transmission efficiency, the case in Fig.9(d.2) that actuating only the top flexible limb is a better option, as it results in a larger force arm compared to the case in Fig.9(d.1). In Fig.9(d.3), both flexible limbs are actuated, resulting in a redundant actuation mode, i.e., using 2 actuators to control 1-DOF motion. This actuation mode offers the best transmission efficiency and load-carrying capacity during motion, as both actuators can contribute to the motion of the manipulator by pushing or pulling the flexible limbs simultaneously. Similarly, for Topology II, we list the 3 actuation modes in (d.4), (d.5), and (d.6), according to the increase of the actuation force transmission efficiency. The modeling method for describing the actuation modes and constrained topologies will be introduced in Sec. 4.3 and 4.4.

In this work, the proposed kineto-static model mainly focuses on the redundant actuation modes, with the aim to analyze the inverse kineto-statics with optimizing the actuation forces distribution. Note that the flexible limbs are also actuated with position control, yet the moving distance is determined with the consideration of the actuation forces' distribution. In addition, considering the high stiffness to weight ratio of truss structures and the fact that the deformation range of flexible limbs are much larger than that of truss structures, the self-weight of the manipulator and the deformation of rigid limbs will be ignored in the following modeling process.

4.1. Governing equations of a large deformation flexible limb

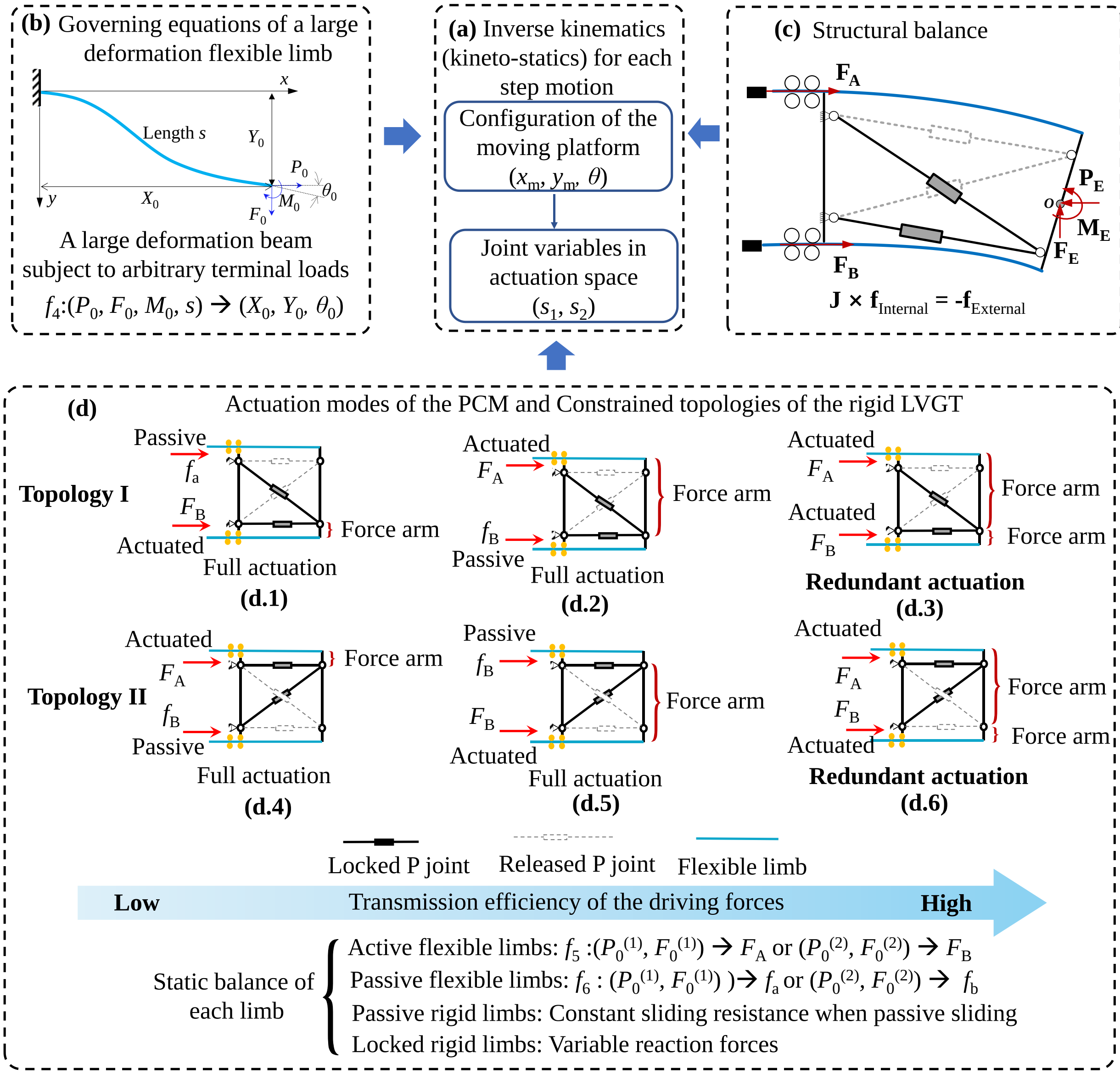

Fig. 9. To establish the inverse kineto-statics model shown in (a), first, the governing equations of large deformation flexible limbs (b) should be established, which could be described as f_4: $\{P_0, F_0, M_0, s\} \rightarrow \{X_0, Y_0, \theta_0\}$, where P_0, F_0, M_0 are load parameters, X_o, Y_o, θ_0 are deflection parameters, and s is the length of the beam. Then, the equations describing (c) the structural balance of the manipulator should be established, which could be revealed by the static balance of the moving platform, written as $\mathbf{J} \times \mathbf{f}_{\text{Internal}} = -\mathbf{f}_{\text{External}}$, where $\mathbf{J}$ is the statics Jacobian matrix, $\mathbf{f}_{\text{Internal}}$ is the vector of scalar internal forces and moments from the LVGT and the PCM, $\mathbf{f}_{\text{External}}$ is the vector of the scalar external forces and moments exerted on the moving platform. At last, the equations describing (d) the actuation modes of the PCM and constrained topologies of the rigid LVGT should be established. In (d.1), the bottom flexible limb is actuated, which allows full control of the manipulator. However, the transmission efficiency of the driving forces is very low for Topology I, due to the short force arm. To improve the transmission efficiency, actuating only the top flexible limb is a better option, as shown in (d.3), since it results in a larger force arm compared to (d.1). In (d.3), both flexible limbs are actuated, resulting in a redundant actuation mode, i.e., using 2 actuators to control a 1-DOF motion. This mode offers the best transmission efficiency and load-carrying capacity during motion, as both actuators can contribute to the motion of the manipulator by pushing or pulling the flexible limbs simultaneously. Similarly, for the constrained Topology II, we list the 3 actuation modes in (d.4), (d.5), and (d.6), according to the increase of the actuation force transmission efficiency.

Since the multiple double rollers could keep the sliding ends of the flexible panels horizontal and can withstand moments, the flexible panels could be viewed as initially straight cantilever beams. The Chained Beam-Constraint-Model (CBCM) is adopted to model the large deformation of the flexible beams considering this approach can model large non-linear deflections of flexible beams at a small cost of computational efficiency [71-73].

In CBCM, a flexible beam is divided into a few Beam-Constraint-Model (BCM) elements [73]. The BCM is based on the *Euler–Bernoulli beam theory*, which can accurately capture the relevant nonlinearities when deflections are within 10% of the beam length. It can provide a compact and closed-form solution for a beam subject to arbitrary end loadings (Fig. 10(a)), which can be simplified expressed as (The specific expressions are given by Eq. (C.1) in Appendix C)

$$\begin{cases} F = f_{\mathrm{BCM1}}(\Delta_y, \alpha, P, S, t, w, E) \\ M = f_{\mathrm{BCM2}}(\Delta_y, \alpha, P, S, t, w, E) \\ \Delta_x = f_{\mathrm{BCM3}}(\Delta_y, \alpha, P, S, t, w, E) \end{cases}, \tag{6}$$

in which S, t, w are the geometry parameters of the beam, standing for the length, in-plane thickness, and out-of-plane thickness, respectively; Δ_x, Δ_y, α are the geometric deflection parameters of the tip of the beam, standing for the axial deflections, transverse deflections, end slope, respectively; P, F, M, are the load parameters on the tip of the beam, standing for transverse force, axial force, and moment M, respectively, as labeled in Fig. 10(a); E is the Young's modulus of the material; f_{BCM1}, f_{BCM2}, f_{BCM2}, are the function operations in the BCM model, the detailed function operations are given in Appendix C.

For large deflection problems (deflections are larger than 10% of the beam length), the beam could be discrete by multiple BCM elements [71-73], as shown in Figs. 10(b) and (c). The discrete number could be estimated by the deformation range of the beam or the thumb formula present in [71]. All these formulas are given in Appendix C.

Totally, there are 6N equations in CBCM, including 3(N-1) equilibrium equations (Eq. (C.4)), 3 geometric constraint equations (Eq. (C.6)), as well as 3N deformation governing equations (Eq. (6)/Eq. (C.1)) of N BCM segments. Using these equations, given any 3 parameters in P_0, M_0, F_0, X_0, Y_0, θ_0, the other 3 parameters could be calculated.

Nonetheless, addressing the IKP for the manipulator still have issues, because geometric deflection parameters, load parameters and the length of the flexible beams are unknown. We need formulate additional constrained equations that reflect the pose and structural balance of the manipulator to solve these unknown parameters.

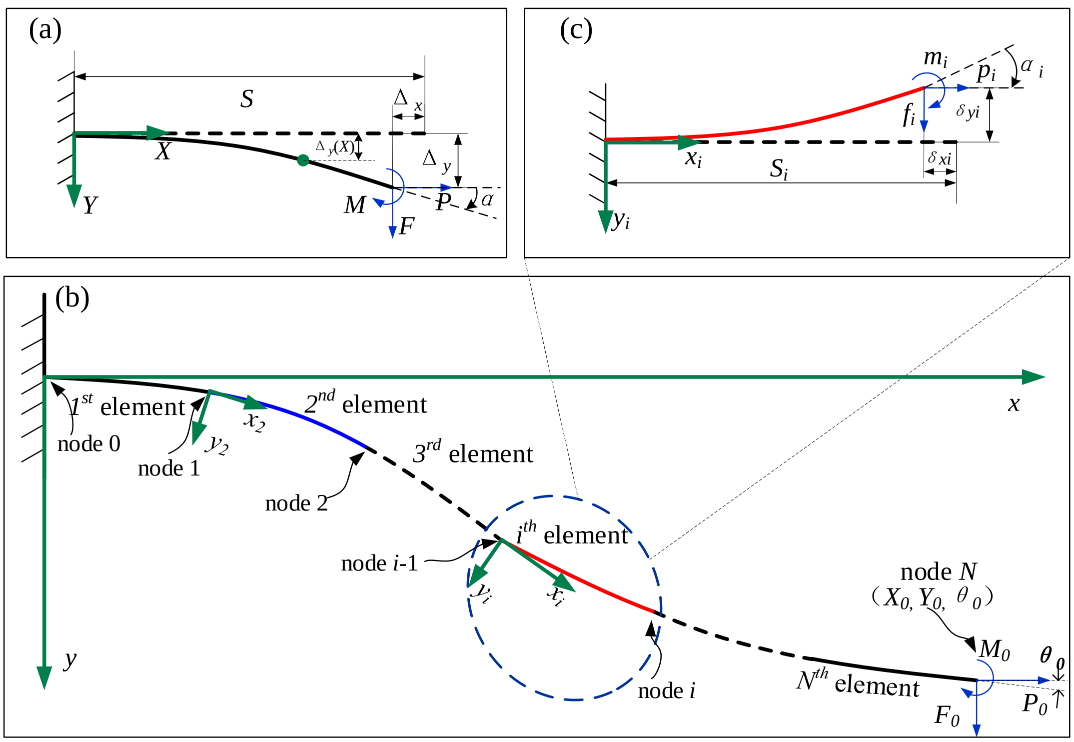

Fig. 10. The mechanic analysis model of a large deformation beam. (a) The beam constrained model (BCM). It could accurately describe the nonlinear deformation of a beam subject to arbitrary end loadings (P, M, F), when the deflections are within 10% of the beam length. (b) The Chained beam constrained model (CBCM). When the deflections are larger than the 10% of the beam length, the beam could be discrete by multiple BCMs. (c) The deformation of the i_{th} element in CBCM.

4.2. Static balance of the moving platform

Referring to the right side of Fig. 11, the structural balance of the mechanism is reflected by the static balance of the moving platform. The moving platform withstands the forces from the internal LVGT $\mathbf{f}_t$ (t=1,2,3,4), the forces and moments form two flexible limbs {$\mathbf{P}_0^{(k)}$, $\mathbf{F}_0^{(k)}$, $\mathbf{M}_0^{(k)}$} (k=1,2), as well as the external forces and moments from the environment {$\mathbf{P}_\mathrm{E}$, $\mathbf{F}_\mathrm{E}$, $\mathbf{M}_\mathrm{E}$}. Therefore, the static equilibrium of the moving platform BD can be expressed as

$$\begin{bmatrix} \mathbf{P}_0^{(1)} + \mathbf{F}_0^{(1)} + \mathbf{P}_0^{(2)} + \mathbf{F}_0^{(2)} + \mathbf{f}_1 + \mathbf{f}_2 + \mathbf{f}_3 + \mathbf{f}_4 + \mathbf{P}_\mathrm{E} + \mathbf{F}_\mathrm{E} \\ (\mathbf{P}_0^{(1)} + \mathbf{F}_0^{(1)})\overrightarrow{\mathbf{BO}} + (\mathbf{P}_0^{(2)} + \mathbf{F}_0^{(2)})\overrightarrow{\mathbf{DO}} + (\mathbf{f}_1 + \mathbf{f}_2)\overrightarrow{\mathbf{V}_4\mathbf{O}} + (\mathbf{f}_3 + \mathbf{f}_4)\overrightarrow{\mathbf{V}_2\mathbf{O}} + \mathbf{M}_0^{(1)} + \mathbf{M}_0^{(2)} + \mathbf{M}_\mathrm{E} \end{bmatrix} = \mathbf{0}, \tag{7}$$

in which all vectors are expressed in the common plane Cartesian coordinate frame $\{\boldsymbol{x}_\mathbf{B}, \boldsymbol{y}_\mathbf{B}\}$; **B**, **D**, **O** represents the upper endpoint, lower endpoint, and midpoint of the moving platform, respectively, as shown Fig. 11.

Equation (7) reflects the relationship between the internal loads and external loads on the manipulator. If we viewed the flexible panels as the joints which can transmit forces as well as moments, Eq. (7) could be written in a more convenient matrix-vector form

$$\left[{}^{\mathrm{B}}\mathbf{J}\right]\{{}^{\mathrm{B}}\mathbf{f}_{\mathrm{IN}}\} = -\{{}^{\mathrm{B}}\mathbf{f}_{\mathrm{EX}}\}, \tag{8}$$

where $\{{}^{\mathrm{B}}\mathbf{f}_{\mathrm{IN}}\}=\left\{P_0^{(1)}\ F_0^{(1)}\ P_0^{(2)}\ F_0^{(2)}\ f_1\ f_2\ f_3\ f_4\ M_0^{(1)}\ M_0^{(2)}\right\}^{\mathrm{T}} \in \mathbb{R}^{10}$ is the vector of scalar internal forces and moments from the LVGT and the PCM, $\{{}^{\mathrm{B}}\mathbf{f}_{\mathrm{EX}}\}=\{P_{\mathrm{E}}\ F_{\mathrm{E}}\ M_{\mathrm{E}}\}^T$ is the vector of the scalar external forces and moments, and $[{}^{\mathrm{B}}\mathbf{J}]$ is the 3×10 statics configuration-dependent Jacobian matrix(expressed in $\{\boldsymbol{x}_\mathbf{B}, \boldsymbol{y}_\mathbf{B}\}$), given as

$$\left[{}^{B}\mathbf{J}\right]=\begin{bmatrix} {}^{\mathrm{B}}\hat{\mathbf{r}}_{\mathrm{P}} & {}^{\mathrm{B}}\hat{\mathbf{r}}_{\mathrm{F}} & {}^{\mathrm{B}}\hat{\mathbf{r}}_{\mathrm{P}} & {}^{\mathrm{B}}\hat{\mathbf{r}}_{\mathrm{F}} & {}^{\mathrm{B}}\mathbf{L}_1 & {}^{\mathrm{B}}\mathbf{L}_2 & {}^{\mathrm{B}}\mathbf{L}_3 & {}^{\mathrm{B}}\mathbf{L}_4 & \mathbf{0} & \mathbf{0} \\ \frac{L_{\mathrm{d}}}{2}\cos(\theta) & \frac{L_{\mathrm{d}}}{2}\sin(\theta) & -\frac{L_{\mathrm{d}}}{2}\cos(\theta) & -\frac{L_{\mathrm{d}}}{2}\sin(\theta) & \frac{h}{2}\sin(\alpha+\beta) & \frac{h}{2}\sin(\beta) & -\frac{h}{2}\sin(\xi) & -\frac{h}{2}\sin(\xi+\gamma) & 1 & 1 \end{bmatrix} \in \mathbb{R}^{3\times 10}, \tag{9}$$

in which ${}^{\mathrm{B}}\hat{\mathbf{r}}_{\mathrm{P}}$ and ${}^{\mathrm{B}}\hat{\mathbf{r}}_{F}$ are unit direction vectors of tangential and normal forces at the fixed end of the flexible panels, ${}^{\mathrm{B}}\mathbf{L}_z$ is the unit vector along the z_{th} (z=1,2,3,4) rigid limb, and $\alpha, \beta, \gamma, \xi$ are angle parameters describing the angles between rigid limbs in LVGT, as shown in Fig. 11. The detailed expressions of these parameters, derived from the geometry parameters of the LVGT, are given in Appendix D.

The inverse pseudo-statics problem involves inverting Eq. (8) to determine the necessary forces and moments from the LVGT and the PCM to support external loads and maintain the manipulator in static equilibrium. Since the statics Jacobian matrix $[{}^{B}\mathbf{J}]$ is non-square and of size 3×10, this problem is underconstrained, which means there exist infinite solutions to the inverse pseudo statics problem.

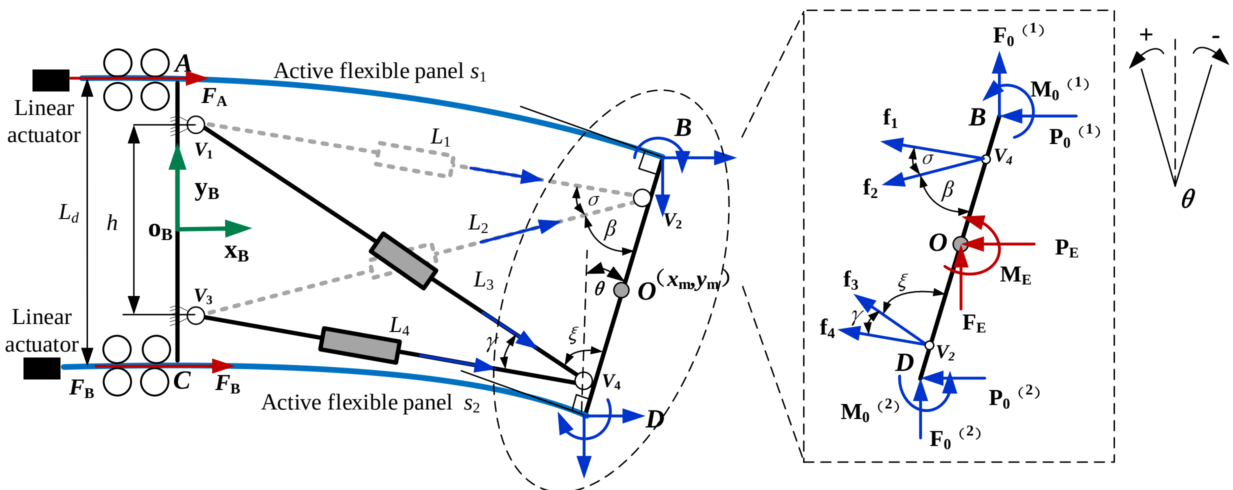

Fig. 11. The force analysis model for the manipulator in an equilibrium state. The structural balance of the mechanism is reflected by the static balance of the moving platform, which withstands the forces from the internal LVGT $\mathbf{f}_t$ (t=1,2,3,4), the forces and moments form two flexible limbs $\{\mathbf{P}_0^{(k)}, \mathbf{F}_0^{(k)}, \mathbf{M}_0^{(k)}\}$ (k=1,2), as well as the external forces and moments from the environment $\{\mathbf{P}_{\mathrm{E}}, \mathbf{F}_{\mathrm{E}}, \mathbf{M}_{\mathrm{E}}\}$.

The common approach to solve the underconstrained linear algebraic problem is to calculate the pseudo-inverse of the statics Jacobian matrix in an optimization manner, minimizing the Euclidean norm of the resulting forces and moments [74]. However, the results obtained by this operation directly are meaningless for this manipulator due to the following reasons:

- For flexible panels, $\{P_0^{(1)}\ F_0^{(1)}\ M_0^{(1)}\}$ and $\{P_0^{(2)}\ F_0^{(2)}\ M_0^{(2)}\}$ should be satisfied with the nonlinear CBCM equations.
- In the LVGT, the released passive P joints cannot provide arbitrary force values.

Therefore, the static balance equation of the moving platform Eq. (8) and the two CBCM equation systems (Eqs. (C.1) ~ (C.6)) of the flexible panels should just be served as a part of the constraint equations in the kineto-static model. These equations could describe the static mechanic model of the flexible limbs as well as the end platform, but they cannot reflect all the mechanical constraint relationships related to each different reconfigured topology of LVGT (Topology I or II) and actuation modes of the PCM (one or two actuators works). Hence, according to the topologies of the LVGT and actuation modes of the PCM, more constraint equations should be established for solving the inverse kineto-static model.

4.3. Constraint equations related to motion topologies

The constraint equations related to the motion topologies of the mechanism can be expressed by the static balance equations of the rigid and flexible limbs, since the parameters in these equations could reflect whether the member is active or passive or locked. For passive members, the sliding resistance forces are constant when the members are passive moving. For active members, the actuation forces are variable. For locked members, the axial reaction forces are variable.

The equations to describe the motion topologies of Topology I and II with s_1, s_2 redundant driven are given as follows

$$\text{Topology I: } f_1 = f_s,\ \ f_2 = f_s, F_A = P_0^{(1)},\ \ F_B = P_0^{(2)}, \tag{10a}$$

$$\text{Topology II: } f_3 = f_s, f_4 = f_s, F_A = P_0^{(1)}, F_B = P_0^{(2)}, \tag{10b}$$

where f_s denotes the constant sliding frictions on the passive members in LVGT, and F_A, F_B denotes the horizontal actuation forces acting on the flexible limbs s_1 and s_2 respectively.

The first two equations in Eqs. (10a) and (10b) stands for the static balance of the released rigid limbs in LVGT, and the last two equations in Eqs. (10a) and (10b) stands for the static balance of the actuated flexible limbs in the horizontal direction.

For the locked limbs in LVGT, they can produce variable reaction forces to satisfy the whole static model of the manipulator, so they have no constrained equations, and we could set them as variable parameters. For example, if we use Eq. (10a) to solve the static model, f_1 and f_2 are known parameters but f_3 and f_4 are not. If we use Eq. (10b) to solve the kineto-statics model, f_3 and f_4 are known parameters but f_1 and f_2 are not. Using these equations, the motion constraints of the different topologies can be described and the actuation force parameters could be introduced into the kineto-static model.

4.4. *Kineto-static model for redundant actuation*

As previously mentioned, the 1-DOF motion is achieved by two active panels working together. The flexible limbs generate coupled deformation with varying internal force distribution, without causing significant motion interference. This characteristic allows for optimization of the two actuation forces distribution. Additionally, we also hope that both actuation forces are minimized.

The weighted sum method [75] is adopted for this multi-objective optimization problem. The specific approach is to set all the constraints discussed in Secs. 4.1~4.3 as the subjected equations and set the force distribution equations as the target equation. The proposed kineto-statics models are given as

For Topology I:

$$\boldsymbol{\tau}_1 = \arg\min\left\{\begin{bmatrix} F_A - F_A^{'} & F_B - F_B^{'} \end{bmatrix} \mathbf{W} \begin{bmatrix} F_A - F_A^{'} \\ F_B - F_B^{'} \end{bmatrix}\right\}$$

$$\text{S.t.}\begin{cases} \left[\text{Eq.(C.1)} \sim \text{Eq.(C.6)}\right]^{\text{T}\ (1)}, \text{Governing equations of } s_1 \\ \left[\text{Eq.(C.1)} \sim \text{Eq.(C.6)}\right]^{\text{T}\ (2)}, \text{Governing equations of } s_2 \\ \text{Eq.(8)},\ \text{Static balance of the moving platform} \\ \text{Eq.(10a), Topology I with PCM redundant driven} \end{cases} \tag{11a}$$

For Topology II:

$$\boldsymbol{\tau}_2 = \arg\min\left\{\begin{bmatrix} F_A - F_A^{'} & F_B - F_B^{'} \end{bmatrix} \mathbf{W} \begin{bmatrix} F_A - F_A^{'} \\ F_B - F_B^{'} \end{bmatrix}\right\}$$

$$\text{S.t.}\begin{cases} \left[\text{Eq.(C.1)} \sim \text{Eq.(C.6)}\right]^{\text{T}\ (1)}, \text{Governing equations of } s_1 \\ \left[\text{Eq.(C.1)} \sim \text{Eq.(C.6)}\right]^{\text{T}\ (2)}, \text{Governing equations of } s_2 \\ \text{Eq.(8)}, \text{Static balance of the moving platform} \\ \text{Eq.(10b)}, \text{Topology II with PCM redundant driven} \end{cases} \tag{11b}$$

where $\mathbf{W}$ is a weight matrix, reflecting the expected contribution ratio of each flexible limb for driving the mechanism, which can be expressed as

$$\mathbf{W} = \begin{bmatrix} W_1 & 0 \\ 0 & W_2 \end{bmatrix} \tag{12}$$

The optimized parameters in Eqs. (11a) and (11b) are $\boldsymbol{\tau_1} = \left\{s_1\ s_2\ F_A\ \ F_B\ \ P_0^{(1)}\ F_0^{(1)} M_0^{(1)}\ P_0^{(2)}\ F_0^{(2)}\ M_0^{(2)}\ f_3\ f_4\right\}^{\text{T}} \in \mathbb{R}^{12\times1}$, $\boldsymbol{\tau_2} = \left\{s_1\ s_2\ F_A\ \ F_B\ \ P_0^{(1)}\ F_0^{(1)} M_0^{(1)}\ P_0^{(2)}\ F_0^{(2)}\ M_0^{(2)}\ f_1\ f_2\right\}^{\text{T}} \in \mathbb{R}^{12\times1}$, in which $s_1\ s_2\ P_0^{(1)}\ F_0^{(1)}\ P_0^{(2)}\ F_0^{(2)}\ M_0^{(1)}\ M_0^{(2)}$ are from the governing equations of the two flexible limbs, F_A and F_B are from the target equations and the constrains equations from Eq. (10). Please note that the differences between Eq. (11a) and (11b) are the optimized parameters ($f_3\ f_4$ or $f_1\ f_2$) and the value of weight matrix $\mathbf{W}$.

For the simulation-based design and off-line motion planning, serials $\mathbf{W}$ can be tried for selecting an optimal group of actuation forces. Besides, $\mathbf{W}$ can also be estimated by considering two following points according to the structure characters of the morphing mechanism. The first one is from the point of view of the transmission efficiency of the driving forces. We can make the actuation limbs with a larger force arm provide more contributions to drive the mechanism. Another aspect to consider is the type of axial forces (actuation forces) applied to the flexible limbs - whether they are tensile or compressive. Since these flexible limbs are located at both sides of the moving platform and rotates around a fixed point on the platform, it follows that one flexible panel will be in tension while the other is in compression. Generally speaking, it is preferable for the tensile limb to contribute more to actuation because the axial driving force generated by a buckling beam is inherently limited.

F_A' and F_B' in Eq. (11) are expected actuation forces. In this study, we expect F_A and F_B to be as small as possible, so we set $F_A' = 0,\ F_B' = 0$.

The above problem described by Eq. (11) is a constraint minimization problem with pure equality constraints, which could be solved by a sequential quadratic programming (SQP) method [76]. In this paper, we adopted the SQP solver in *fmincon* function from MATLAB 2019B to solve this model. In general, the inverse kineto-static model could be solved in the following sequence:

1) For a given desired pose (x_m, y_m, θ) of the moving platform, the minimum number of steps and each intermediate states (n, ${}^0\theta_1$, ${}^1\theta_2$, ${}^2\theta_3$... ${}^{n-1}\theta_n$) are determined by the optimization model Eq. (5).
2) Then, each intermediate pose of the moving platform could be served as the input to the inverse kinematic model Eqs. (D.3) ~ (D.5) to calculate the boundary geometry parameters of flexible limbs (the coordinates of point B and D, and the deflection angle θ), as well as the geometry parameters of the LVGT ($\alpha, \beta, \gamma, \xi, L_1, L_2, L_3, L_4$).
3) The above parameters could be served as the inputs to the optimization model Eq. (11). Through solving the model, the forces exerted on the moving platform $\left\{P_0^{(1)}\ F_0^{(1)}\ P_0^{(2)}\ F_0^{(2)}\ f_1\ f_2\ f_3\ f_4\ M_0^{(1)}\ M_0^{(2)}\right\}$, the actuation forces $\{F_A, F_B\}$ and the extended length of the two flexible limbs $\{s_1, s_2\}$ could be obtained. Besides, using the theses parameters, we can simulate the shapes of flexible limbs through Eq. (C.3).

5. Simulations and experiments

In this section, we present case studies that serve to demonstrate the effectiveness of the proposed kineto-static model for redundant actuation and the multi-step kinematic model. Both models are verified using nonlinear FEA and experimental tests. Additionally, we investigate the influence of LVGT dimension on actuation forces and actuation distance using the proposed kineto-static model.

5.1. Inverse kineto-static simulation of full or redundant actuation

The inverse kineto-static analysis for redundant actuation is performed on Topology I, since essentially, Topologies I and II are symmetrical. The key geometry and mechanical parameters of the manipulator are given in Tab. 1. These parameters are the same as those in the fabricated prototype shown in Sec 5.3.

Table 1. The main geometry and material parameters of the manipulator

Moving platform	L_d (mm)	205	
	h (mm)	130	
Rigid limbs	L_1, L_4 (mm)	Inital:285	Range: 285~500
	L_2, L_3 (mm)	Initial:313.25	Range: 313.25~550
Flexible limbs	s_1, s_2 (mm)	Initial:300	Range:280~600
	w (mm)	135	
	t (mm)	0.98	
	E (Gpa)	45	
	Poisson ratio γ	0.30	

The main goal of the inverse kineto-static model is to obtain the required actuation distance and actuation forces for a desired pose of the moving platform. We give the calculation results of the actuation forces (Fig. 13) and extended length (Fig. 14) of the actuated flexible limbs for Topology I by using Eq. (11a). In these calculations, the deflection angle of the moving platform changes from 0 ° to 30 °, considering that too much bending will result in the motion interference between flexible limbs and rigid limbs. The load condition is set at as {P_E, F_E, M_E} = {–20 N, –10 N, 3 Nm}. The number of the BCM element is set as 3 based on two factors. First, we considered the potential deflection range of the flexible limbs, noting that the BCM is accurate when the deflection is within 10% of the beam length. Second, through the initial experimental and FEA results, we observed no more than 3 inflection points. Additionally, we set the friction force of the released lockable limbs to zero (f_s=0).

We tried different values of W_1 and W_2 to observe the differences in the actuation forces (Fig. 13) and actuation distance (Fig. 14). These values of **W** are given as (W_1, W_2) = (0, 1), (4.5, 1), (20, 1), (40, 1), (80, 1), (1, 0), for which the ratio W_1/W_2 increases as 0, 4.5, 20, 40, 80, and +∞. The ratio 4.5 is calculated by the force arm ratio of the two flexible limbs, i.e., $\frac{h+(L_d-h)/2}{(L_d-h)/2}$. The ratio 0 indicates that we just use flexible limbs s_1 for actuation, and +∞ means we just use flexible limb s_2 for actuation.

The results of our calculations were verified using nonlinear FEA. We created a Standard/Explicit model using ABAQUS 2020 and adopted Static/General analysis steps. The boundary conditions for our FEA model are shown in Fig. 12(a) and (b). To simplify our model and make it easier to converge and reduce computation time, we replaced the constraints from multiple sets of rollers with fixed blocks having through slots. The constraints from the LVGT can be set as an R joint, as illustrated in Fig. 12(a). The meshed model and its deformation shapes are shown in Fig. 12(c), in which the C3D8R units are adopted for areas of possible contact and C3D20R units are adopted for other places. Besides, a finer mesh is generated in the area near the connection between flexible limbs and the rigid moving platform. Generally speaking, coarse grids in this study have a long side length of approximately 8-15 mm, while fine grids have a long side length of approximately 2-5 mm. Besides, 3-5 seeds are used in the thickness direction of the flexible panels for meshing.

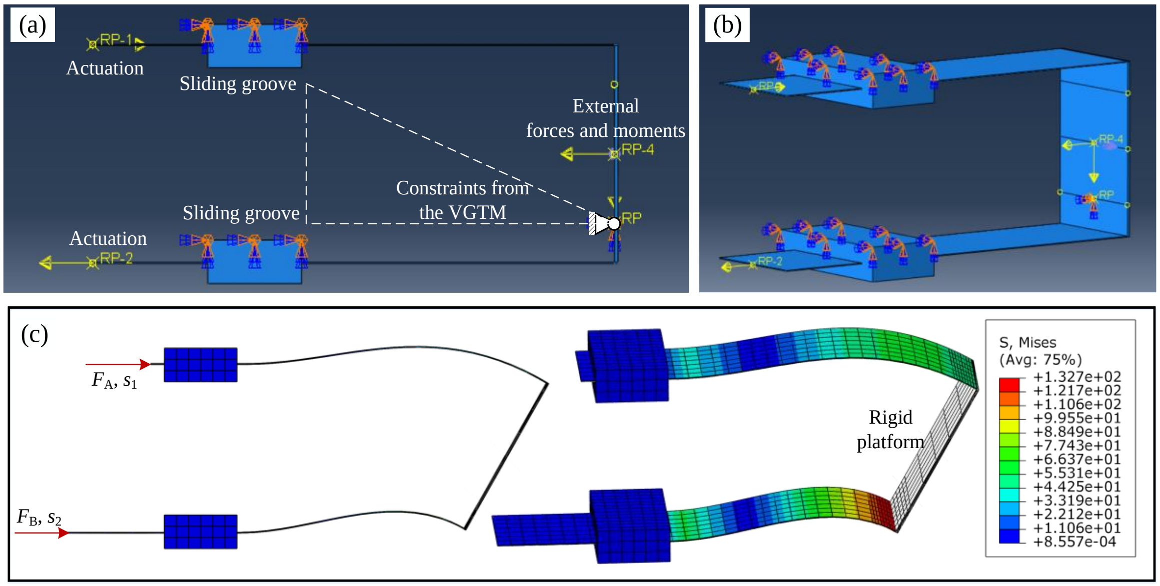

Fig. 12. The FEA model in ABAQUS. (a) and (b) show the boundary condition settings. We replaced the constraints from multiple sets of rollers with fixed blocks having through slots, to simplify our model and make it easier to converge and reduce computation time. The constraints from the LVGT can be set as an R joint, as illustrated in (a). (c) shows the meshed model and the mises stress contour plot.

The inputs for the FEA model could be either the calculated moving distance of the flexible limbs, with the outputs being the poses of the moving platform and the reaction forces (actuation forces) on the input sides. Alternatively, the inputs could be the calculated actuation forces, with the outputs being the moving distance of the flexible limbs and the poses of the moving platform. We tried

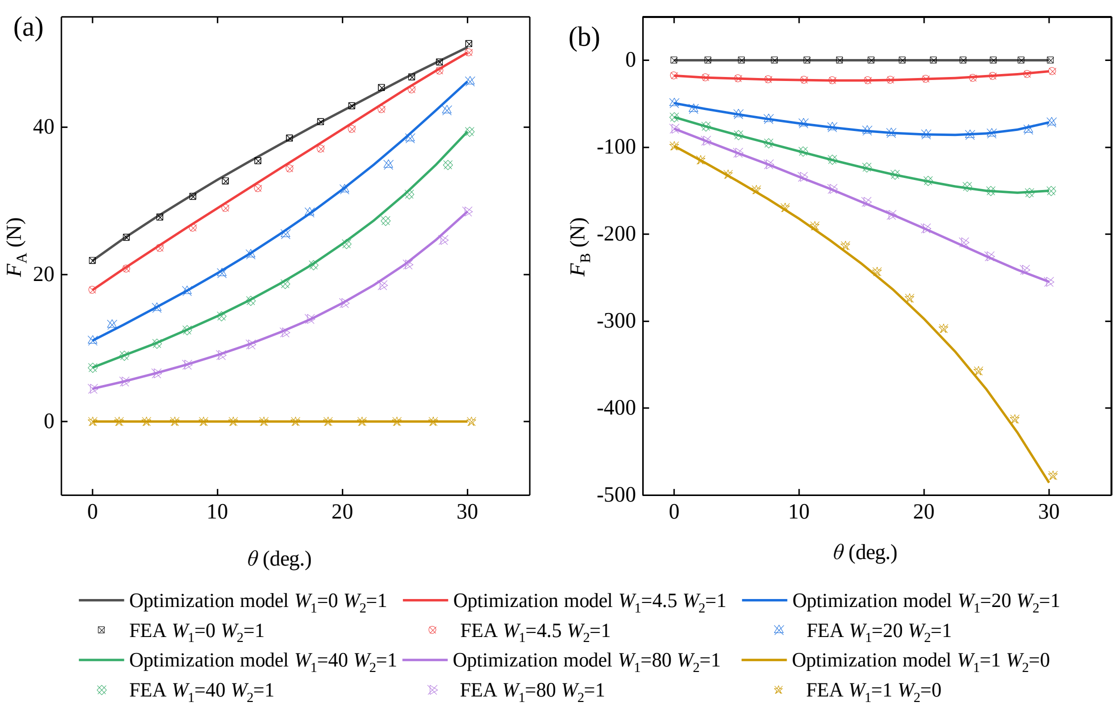

Fig. 13. The calculated and non-linear FEA results of the actuation forces under the load conditions $\{P_E, F_E, M_E\}$ ={–20 N, –10 N, 3 Nm} in different actuation strategies (different sets of W_1, W_2). The difference of the ratio W_1/W_2 means that the contribution of flexible limbs in the driven process are different. For example, W_1=0, W_2=1 stands for the full actuation case that just s_1 works; W_1=1, W_2=0 is for s_2 full actuation; and W_1=80, W_2=1 stands for the redundant actuation mode that expects s_2 as the main actuation. (a) gives the results for F_A. (b) gives the results for F_B.

both methods, and the latter one yielded more stable convergence results. In each simulation, we created 13 analysis steps and recorded the actuation forces, actuation distance, and the poses of the moving platform in these 13 static equilibrium states. The results are plotted in Figs. 13 and 14. From the results in Figs. 13 and 14, we can observe that:

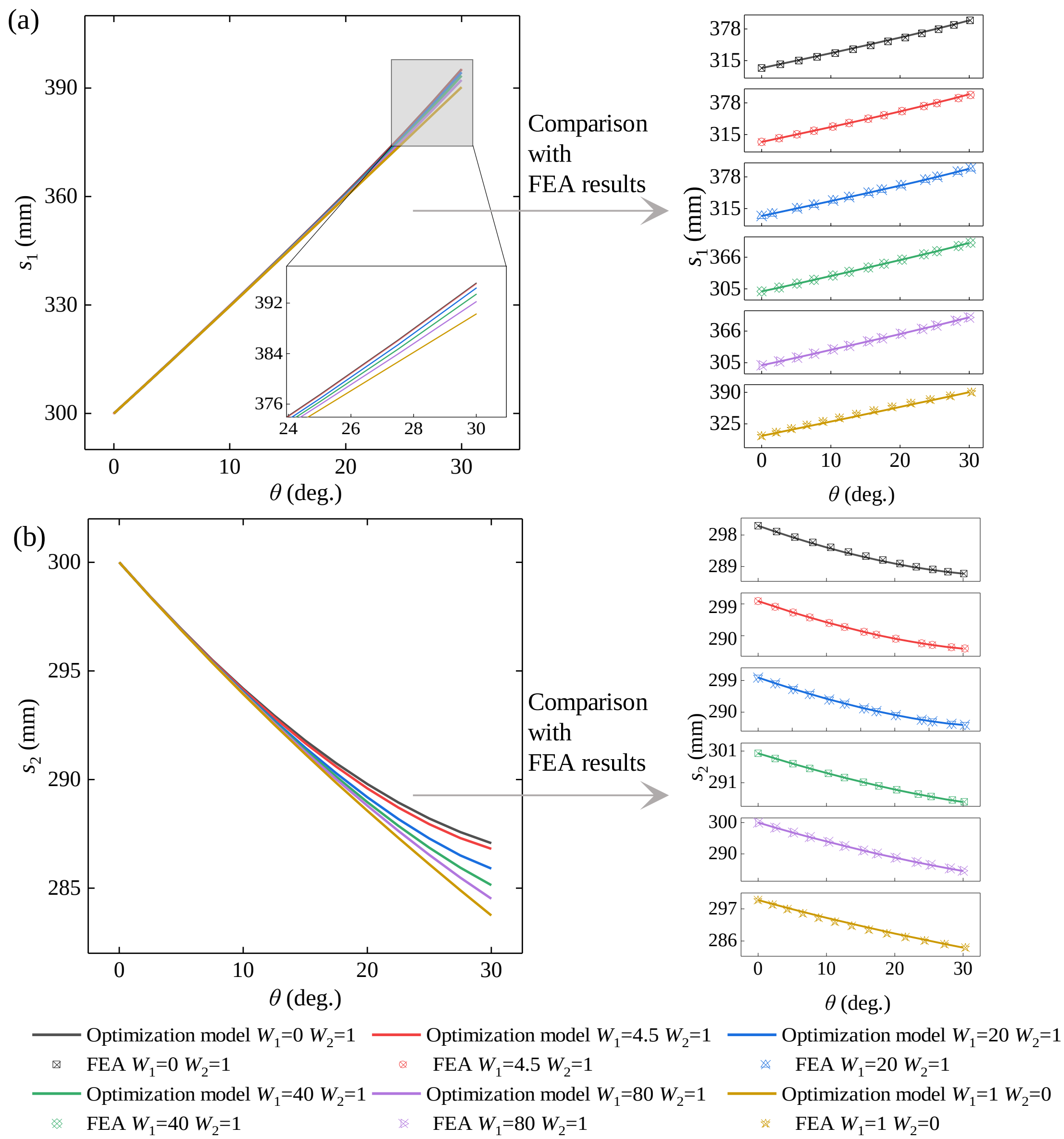

Fig. 14. The calculated and non-linear FEA results of the extended length of flexible limbs under the loading conditions $\{P_E, F_E, M_E\}$ = {–20 N, –10 N, 3 Nm} in different actuation strategies (different sets of W_1, W_2). (a) gives the results of s_1 from the optimization model (left) and the comparison with the results from FEA (right). (b) gives the results of s_2 from the optimization model (left) and the comparison with the results from FEA (right).

- The proposed model can accurately calculate the required actuation forces and required actuation distances under external end loads. For actuation forces, the average error is around 2.8% for F_A and 3.5% for F_B, compared with FEA results. For actuation distance, the average error is less than 1% for both s_1 and s_2 compared with the FEA results. The model is more accurate at predicting actuation distance compared with that of actuation forces. The error could come from the inherent error of the CBCM model and the inherent differences between the two computation methods.
- Redundant actuation can significantly change the actuation forces and their distributions (Fig. 13), by adjusting the extended length of the flexible limbs. Referring to Fig. 13, when we apply different weight coefficients and set the rotation angle equal to 30°, the actuation force F_A varies within 0~50.9 N, and F_B varies within −150.0~0 N. (The minus means the direction of the force is to the left, representing tension force on the flexible panel.) The wider range of F_B variation is due to the smaller force arm of s_2, requiring more actuation force to drive the mechanism.
- For this case study, using s_1 as the main driving limb is more favorable since small driven forces can be obtained for both

actuations. As shown in Fig. 13, when W_1=1, W_2=0, the maximum actuation forces are F_{A_max} = 50.8 N, F_{B_max}= 0 N; When W_1= 4.5, W_2=1, the maximum actuation forces are F_{A_max}= 50.2 N, F_{B_max}= –12.7 N. For other cases, the maximum actuation force of F_A will be decreased, but F_B will increase a lot. Among the results in Fig. 13, when W_1=20, W_2=1, F_{B_max}= –71.1 N; When W_1=40, W_2=1, F_{B_max}= –150.0 N; When W_1=80, W_2=1, F_{B_max}= –254.6 N; When W_1=1, W_2=0, F_{B_max}= –485.4 N. The reason for this phenomenon is that the actuation force arm of s_2 is very small. The force arm is related to the dimension of the LVGT, i.e., the value of h labeled in Fig. 11. We will investigate the influence of the dimension of the LVGT on the driven forces and driven distance in the next section.

- When the weight matrices are different, the changes in driving distance are relatively small (Fig. 14(a) and (b)), but the changes in driving forces are very large (Fig. 13). This indicates that though there is no strong motion interference of the redundant actuated flexible limbs, the influences on internal forces on flexible limbs could be very large. Therefore, if position control is applied, a relatively high position accuracy of the actuator is required, and the actuator should be able to provide a larger driving force to compensate for the increased driving force generated by position control errors. Alternatively, force sensors could be added to implement force control or force/position hybrid control.

5.2. *Characteristics analysis with different LVGT dimensions*

Different truss dimensions (Fig. 15) will result in differences in the two actuation force arms, thus further affecting the driving forces and driving distance. Essentially, the difference between the two actuation force arms can be reflected by the ratio of the height of the LVGT and the height of the moving platform, i.e., h/L_d. To investigate the influence of the LVGT dimension on the actuation forces and distance, we plotted the calculation results of the actuation forces/distance with respect to h/L_d in Fig. 16. In our simulation, the rotation angle of the moving platform θ is set as 30 °, and a simple load condition [0, 0, 0] is applied. The range of h/L_d is [0.05, 0.8] since if this ratio is too large, the rotation angle of the moving platform will be very limited. Four weight matrices are investigated, which correspond to 4 typical actuation strategies: (1) Just using s_1 for actuation (W_1=0, W_2=1, as shown in Fig. 15(**a**) and (**b**)). (2) Just using s_2 for actuation (W_1=1, W_2=0, as shown in Fig. 15(**c**) and (**d**)). (3) Using s_1 as the main actuation (W_1=1, W_2=20, as shown in Fig. 15(**e**) and (**f**)). (4) Using s_2 as the main actuation (W_1=20, W_2=1, as shown in Fig. 15(**g**) and (**h**)).

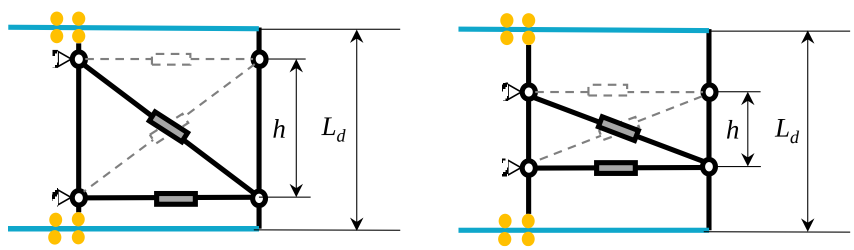

Fig. 15. The illustration of different truss dimensions (Topology I). Different truss dimensions will result in differences in the two actuation force arms, thus further affecting the driving force and driving distance. Essentially, the difference between the two actuation force arms can be reflected by the ratio of the height of the LVGT and the height of the moving platform, i.e., h/L_d.

From the results in Fig. 16, we can observe that:

- The dimension of the LVGT has significant influences on the driving forces and distances of the flexible limbs. When the rotation angle of the moving platform is fixed, as the h/L_d increases, the extended length of s_1 and s_2 are both increased (Figs. 16(b) (d) (f) and (h)), and the actuation forces are also changed. Generally speaking, if the actuation force arm of a flexible limb is larger than the other one, when we set a smaller weight coefficient to it (expect it as the main actuation limb since a smaller weight coefficient will make it provide more actuation force), with the increase of h/L_d, the force of the main driving limb will be decreased (F_A in Figs. 16(a) and (e)), and the actuation force of secondary driving limb will be slightly increased (F_B in Fig. 16 (e)). However, if we apply a very small weight coefficient to the flexible limb with a smaller force arm (expected it as the main actuation limb), a small actuation force can be obtained on the other flexible limb (F_A in Fig. 16(c) and (g)), while the actuation force on the main actuation flexible limb could be very small or very large (F_B Fig. 16(c) and (g)), since small changes in the overall balance state of the manipulator may cause large changes in the force on the flexible limb with a smaller force arm.
- From the point of view of reducing the actuation forces in redundant actuation modes, we recommend selecting a LVGT with relatively large dimensions and using a flexible limb with a longer actuation force arm as the main actuation (Fig. 16(e) and (g)).

5.3. *Experimental setup*

The fabricated prototype and the experiment setup are introduced in this section. The main parts of the prototype (Fig. 17 (a)) consist of 9 passive rigid limbs (each made by aluminum alloy telescopic sleeves with manual cam mechanisms as lockable devices), 2 actuated flexible limbs (made by carbon fiber reinforced polymer (CFRP)), a moving platform (made by Nylon boards), a base platform (made by aluminum alloy boards), 4 sets of double rollers with bearings (MISUMI RORELAG28-T3-8-100), two linear slide modules with motors (MISUMI KUA1210-640-150), and an aluminum alloy frame. All the rigid limbs are connected with platforms through aluminum alloy R joints. The distal ends of the two flexible limbs are fixed on the edge of the moving platform with two rows of bolts to keep the limbs strictly perpendicular to the moving platform, which is the same as the modeling assumptions in mathematical models. The other ends of the flexible limbs are connected with the sliding moving platform in the

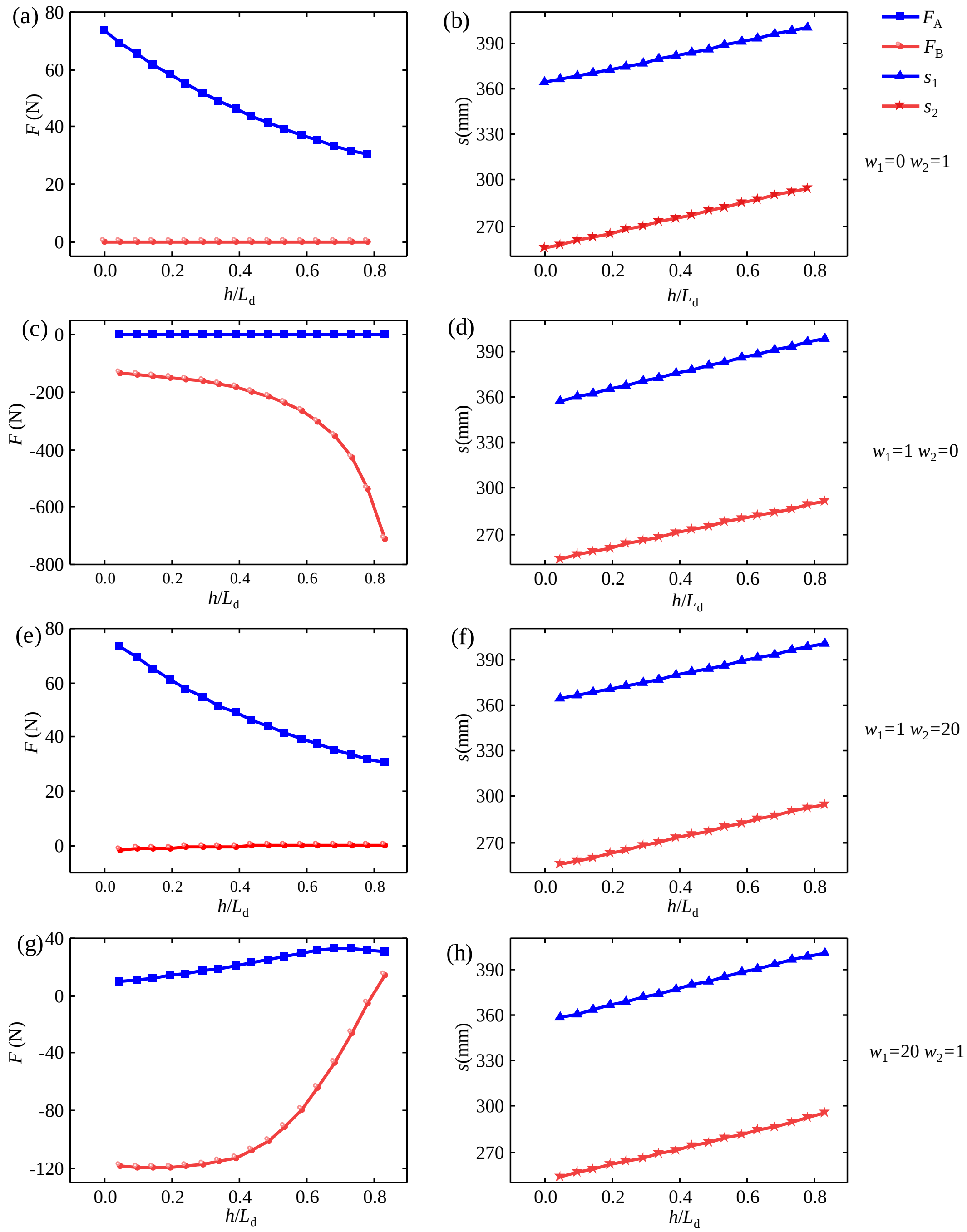

Fig. 16. The required auction forces and distance of the flexible limbs with different truss dimensions. In our simulation, the rotation angle of the moving platform θ is set as 30 °, and a simple load condition [0, 0, 0] is applied. The range of h/L_d is [0.05, 0.8] since if this ratio is too large, the rotation angle of the moving platform will be very limited. Four weight matrices are investigated, which correspond to 4 typical actuation strategies: (1) Just using s_1 for actuation (W_1=0, W_2=1 in (a) and (b)). (2) Just using s_2 for actuation (W_1=1, W_2=0 in (c) and (d)). (3) Using s_1 as the main actuation (W_1=1, W_2=20, in (e) and (f)). (4) Using s_2 as the main actuation (W_1=20, W_2=1 in (g) and (h)).

linear slide modules. The main geometry and material parameters of the manipulator are already given in Tab. 1.

Our experimental platform primarily tests the motion distances of two linear actuations and the actuation forces under given the pose of the moving platform and the end-load conditions, with the aim of verifying proposed kineto-static models. As shown in Figs. 17(a), the moving distances of the flexible limbs are measured by digital display grating rulers (WD-5450-600mm, with resolution 0.01 mm, accuracy 0.15 mm), and the actuation forces are measured by two force gauges (IMADA DST-50N, resolution 0.01 N, accuracy 0.11 N). The poses of the moving platform are measured by an optical measurement (NDI Polaris, with accuracy

0.12 mm), as shown in Fig. 17 (b). Some weights are hanging in the middle of the moving platform (Fig. 17(c)) to simulate the external loads. The key location points and the coordinate systems used in kineto-static analysis are given in Fig. 17(d).

Note that, although our loading method by hanging objects is simple, any external force generated along the direction of the moving platform will ultimately be withstand by the fixed point on the moving platform, which does not affect the driving force and displacement. Therefore, as long as the loading method can change the force perpendicular to the direction of the moving platform, the impact of different end loads on the driving force and displacement can be obtained. As shown in Fig. 17(e), the experimental load $\mathbf{F}_{exp}$ can generate a component force $\mathbf{F}_{exp\_M}$ along the direction of the moving platform and a component force $\mathbf{F}_{exp\_Vm}$ perpendicular to the direction of the moving platform.

Besides, due to the limited locking force of the lockable joint (constructed by some manual cam mechanisms) used in our experimental prototype and the limited width of the mechanism (thickness of the mechanism outside the morphing plane), we did not apply very large loads in experiments. If we want to further improve the potential load carrying ability of this design, we could optimize the number of the morphing units of the LVGT [77] (as illustrated in Fig. 17(f)), or develop small lockable P joints with high locking load [44, 45], which were investigated in our previous studies [44, 45, 77].

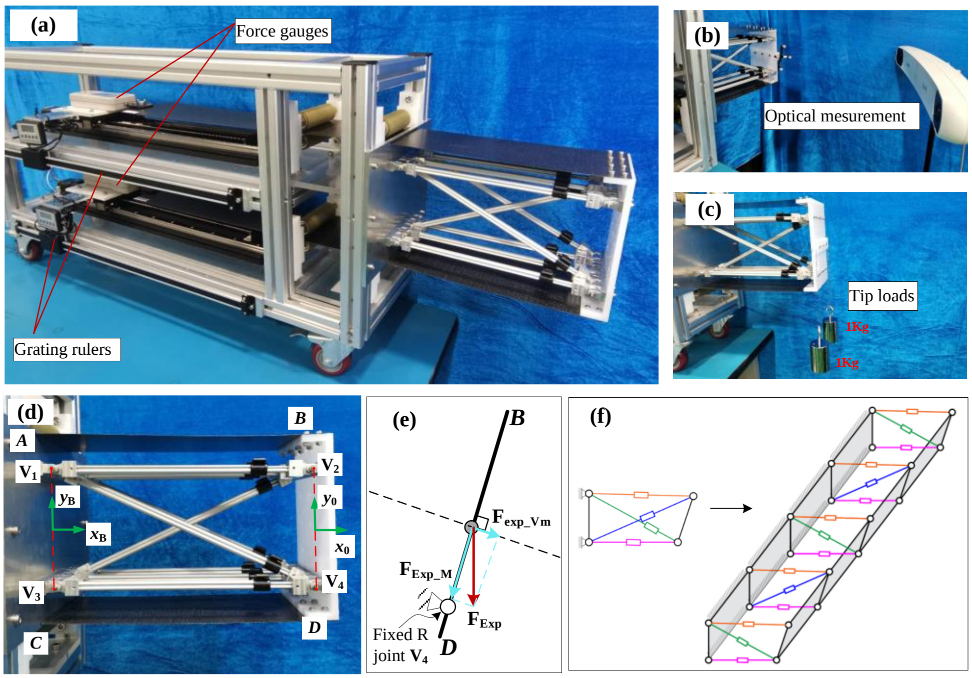

Fig. 17. The prototype and experimental setup. (a) shows the prototype and the sensors to test the actuation forces and actuation distance. The main parts of the prototype consist of nine passive lockable rigid limbs, two actuated flexible limbs, a moving platform, a base platform, four sets of double rollers with bearings, two linear slide modules with motors, and an aluminum alloy frame. The moving distances of the flexible limbs are measured by digital display grating rulers, and the actuation forces are measured by two force gauges. (b) shows the experimental set up to test the pose of the end platform by using an optical measurement. (c) shows that we use weights hung in the center of the moving platform to simulate external forces. (d) shows the coordinate systems setup on the prototype. (e) illustrates that the experimental load $\mathbf{F}_{exp}$ can generate a component force $\mathbf{F}_{exp\_M}$ along the direction perpendicular to the moving platform and a component force $\mathbf{F}_{exp\_Vm}$ perpendicular to the direction of the moving platform. However, the component force along the direction of the moving platform will ultimately be withstand by a fixed point on the moving platform (V_4), which will not affect the actuation forces and distance on flexible limbs. (f) illustrates that the potential load carrying ability of the manipulator can be improved by optimizing the number of the morphing units of the LVGT.

5.4. *Experimental verification for multi-step motion kinematics*

This section aims to verify the multi-step kinematics model proposed in Sec. 3 by experiments. Four case studies are conducted, as shown in Tab. 2. Using the multi-step kinematics model, we determined the required topology switching and the rotation angle for each step motion according to the final desired pose of the moving platform. The results, along with the poses of the moving platform after each step motion, are presented in Tab. 2.

For the experiments, an optical measurement is used to test the pose of the moving platform, ensuring that each step motion achieves the desired rotation angle of the end platform. After the multi-step motion, the final experimental poses are given in Tab. 2. By comparing it with the desired pose, we can observe that using the calculated results, the prototype can reach the desired poses with a very small motion error. The mean, maximum, and median percentage error between the theoretical results and the experimental results are given in Tab. 2. Among these studied cases, the maximum position (distance) error ($e_{dis} = \sqrt{e_x^2 + e_y^2}$) of the end platform is 2.95mm, and the maximum percentage error of the position $(e_{dis}/\sqrt{\Delta x^2 + \Delta y^2})$ is 0.75%, where the Δx and

Table. 2. Inverse kinematics results of the multi-step motion with topology reconfiguration (Units: mm, deg.)

		Case 1	Case 2	Case 3	Case 4
Initial pose $(x_\mathrm{m}, y_\mathrm{m}, \theta)$		(285,0,0)			
Desired pose $(x_\mathrm{m}, y_\mathrm{m}, \theta)$		(450,10,30)	(435, -15, -5)	(385,10,15)	(350, -10, -20)
Less steps (n)		4	4	3	3
Topology switching		I⟶II⟶I⟶II	I⟶II⟶I⟶II	II⟶I⟶II	I⟶II⟶I
Rotation angle ($^0\theta_1$, $^1\theta_2$, $^2\theta_3$, $^3\theta_4$)		(17.08, 42.67, 42.67, 47.08)	(24.77, 45.83, 45.83, 19.77)	(24.09, 37.48, 28.39)	(17.66, 19.13, 21.47)
The pose of each step motion $(x_\mathrm{m}, y_\mathrm{m}, \theta)$	Step 1	(304.09, –2.87, –17.08)	(312.23, –5.98, –24.77)	(311.53, 5.66, 24.09°)	(304.72, –3.06, –17.66)
	Step 2	(351.25, 0.65, 25.59)	(362.82, –7.16, 21.06)	(353.12, 9.56, –13.39)	(326.11, –6.11, 1.47)
	Step 3	(398.41, 4.16, –17.08)	(413.42, –9.26, –24.77)	(385.00, 10.00, 15°)	(350, –10, –20)
	Step 4	(450.00,10.00, 30.00)	(435, –15, –5)	\	\
Experimental final pose		(451.50, 10.70, 30.22)	(436.12, –15.76, –5.08)	(387.9, 10.53, 15.11)	(349.2, –9.18, –19.61)

Position error (%)		**Orientation error (%)**	
Mean	**0.40**	**Mean**	**1.25**
Max	**0.75**	**Max**	**1.99**
Median	**0.30**	**Median**	**1.15**

Δy are the required moving distance of the desired pose in x and y directions respectively. The maximum orientation (angel) error of the moving platform ($e_\theta = \sqrt{e_\theta^2}$) is 0.39° and the maximum percentage error of the orientation ($e_\theta/\sqrt{\theta^2}$) is 1.99%. Note that, in these experiments, the nonlinear deformation of the flexible limbs is not taken into count, and we use the external optical sensors to maintain the motion accuracy of each step motion. Therefore, the motion error mainly comes from the machining error of mechanical members, and the transmission error of the moving pairs.

5.5. Experimental verification of the kineto-static model

This section verifies the kineto-statics model presented in Sec. 4 by experiments. In the simulation, all the motion steps in Tab. 2 are analyzed with loading conditions $\{^\mathrm{B}\mathbf{F}_\mathrm{EX}\} = \{0\ -19.6\mathrm{N}\ 0\}^\mathrm{T}$, which are equal to our experiments. Table 3 gives the details of the kineto-static analysis results, including the required extended length of the actuated flexible limbs and the actuation forces. The weight coefficients are set as W_1=1, W_2=4.5 for Topology I, and W_1=4.5, W_2=1 for Topology II, in which 4.5 is the force arm ratio of the main actuation flexible limb to the secondary actuation limb. The main actuation flexible limb is the one having a larger actuation force arm.

In each experiment, the flexible limbs are driven to the calculated desired extended length. As shown in Fig. 17(a), two granting rulers with digital displays are used to keep the motion accuracy of the flexible limbs. The pose of the moving platform is measured by the optical measurement, capturing the tracked object fixed in the middle of the moving platform (as shown in Fig. 17(b)). At last, we can obtain the actuation forces through force gauges (Fig. 17(a)). The configurations of the prototype after each step motion for case 1 are also given in Fig. 19.

The experiment for each desired pose was repeated 5 times. The mean experimental results and the maximum, mean, and medium relative error of the poses and actuation forces are recorded in Tab. 3. Besides, the mean absolute error with the error bar (standard deviation) of each experimental pose for the studied cases are given in Fig. 18.

From the results in Tab. 3, Figs. 18 and 19, it can be seen that:

- The proposed model can accurately calculate the required moving distance and actuation forces of the flexible limbs (Tab. 3 and Fig. 18), as well as predict the shape of the manipulator (Fig. 19). From the results in Tab. 3 and Fig. 18, we can also obtain that when implementing open-loop position control of the actuator, the mean position and orientation (angle) relative error of the end platform are less than 4% and 7% respectively; and the mean absolute error are less than 2mm and 0.53 ° respectively, which means that the proposed model can be applied to realize relatively high-accuracy position control.

Table. 3. Kineto-static analysis results of each motion step. (Units: mm, deg., N)
($W_1 = 1$, $W_2 = 4.5$ for Topology I and $W_1 = 4.5$, $W_2 = 1$ for Topology II)

		Poses of the moving platform (Calculation) $(x_{\mathrm{m}}, y_{\mathrm{m}}, \theta)$	Poses of the moving platform (Experimental) $(x_{\mathrm{m}}, y_{\mathrm{m}}, \theta)$	Extended length of flexible limbs and actuation forces (Calculation) $(s_1, s_2, F_{\mathrm{A}}, F_{\mathrm{B}})$	Extended length of flexible limbs and actuation forces (Experimental) $(s_1, s_2, F_{\mathrm{A}}, F_{\mathrm{B}})$
Case 1	Step 1	(304.09, – 2.87, 17.08)	(304.15, – 2.95, –17.12)	(351.42, 290.76, 18.93, – 0.57)	(351.42, 290.76, 17.62, – 0.62)
	Step 2	(351.25, 0.65, 25.59)	(351.01, 0.62, 25.42)	(326.91, 417.88, – 0.45, 31.31)	(326.91, 417.88, – 0.58, 32.72)
	Step 3	(398.41, 4.16, – 17.08)	(398.81, 4.08, – 17.23)	(446.64, 385.96, 15.36, – 0.36)	(446.64, 385.96, 16.45, – 0.42)
	Step 4	(450.00, 10.00, 30)	(450.95, 9.85, 29.85)	(421.70, 531.18, – 0.02, 26.28)	(421.70, 531.18, – 0.23, 27.83)
Case 2	Step 1	(312.23, –5.98, –24.77)	(312.68, –6.12, –25.21)	(375.61, 288.05, 26.49, –0.53)	(375.61, 288.05, 27.58, –0.75)
	Step 2	(362.82, –7.16, 21.06)	(361.51 –6.53, 20.53)	(344.94, 419.66, –0.50, 26.83)	(344.94, 419.66, –0.8, 27.59)
	Step 3	(413.42, –9.26, –24.77)	(414.23, –10.13, –25.12)	(478.48, 390.35, 18.18, –0.23)	(478.48, 390.35, 17.25, –0.12)
	Step 4	(435, –15, –5)	(436.22, –15.82, –5.32)	(459.34, 441.45, 0.16, –2.83)	(459.34, 441.45, 0.56, –3.2)
Case 3	Step 1	(311.53, 5.66, 24.09)	(310.91, 5.35, 23.89)	(288.25, 373.72, –0.66, 31.66)	(288.25, 373.72, –0.52, 32.85)
	Step 2	(353.12, 9.56, –13.39)	(354.26, 9.83, –13.67)	(393.73, 346.19, 15.67, –0.47)	(393.73, 346.19, 15.96, –0.75)
	Step 3	(385.00, 10.00, 15)	(384.12, 9.85, 14.75)	(375.08, 428.68, –0.44, 14.86)	(375.08, 428.68, –0.82, 15.81)
Case 4	Step 1	(304.72, –3.06, –17.66)	(305.34, –3.15, –17.85)	(353.21, 290.52, 19.50, –0.57)	(353.21, 290.52, 20.71, –0.68)
	Step 2	(326.11, –6.11,1.47)	(325.21, –6.02, 1.41)	(338.58, 343.84, –0.19, 4.02)	(338.58, 343.84, –0.45, 4.89)
	Step 3	(350, –10, –20)	(350.56, –10.29, –20.29)	(403.66, 332.53, 17.16, –0.42)	(403.66, 332.53, 18.56, –0.95)

Position error (%)		**Orientation error (%)**		**Actuation force error (%)**	
Mean	**1.34**	**Mean**	**2.13**	**Mean**	**6.19**
Max	**3.14**	**Max**	**6.40**	**Max**	**14.29**
Median	**0.98**	**Median**	**1.41**	**Median**	**5.71**

- From the results in Tab. 3, it can be observed that the expected main actuation limbs can provide much more driven forces, and the secondary actuation limb just provides very small actuation forces, which fits the experimental results well. The percentage error of the actuation force is less than 15%, which is relatively large in some experimental poses. Note that the force error is obtained from the data larger than 1 N since if the force is near zero, it is very close to the resolution and accuracy of the force gauge, which will probably lead to excessive measurement error. We believe that the error in the driven forces mainly comes from the fabricated dimension error of the prototype, the assumption of not considering the weight of the mechanism in the theoretical model, and the additional force caused by actuation distance error in redundant actuated flexible limbs.

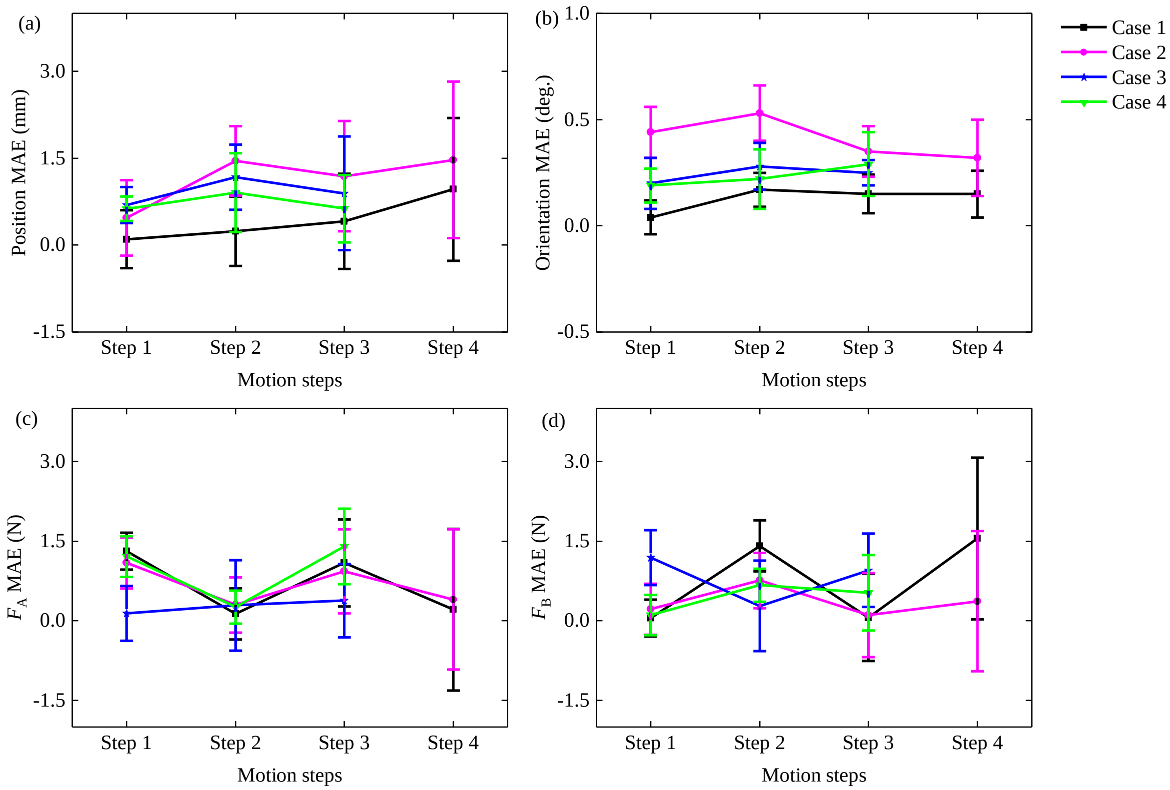

Fig. 18. The mean absolute error (MAE) and standard deviation of the pose of the moving platform and the actuation forces. (a) The MAE of the position of the moving platform. (b) The MAE of the orientation of the moving platform. (c) The MAE of the actuation force F_A. (d) The MAE of the actuation force F_B.

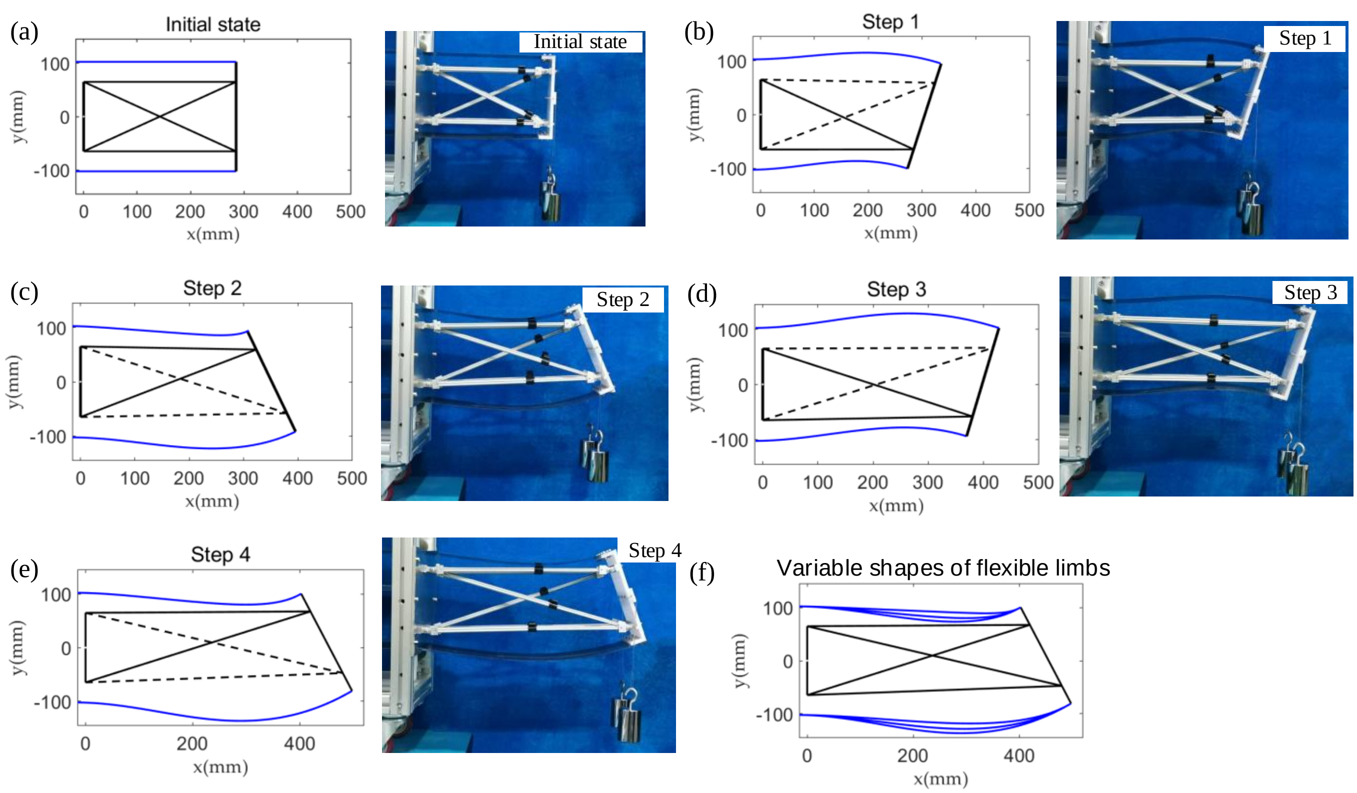

Fig. 19. The simulated and experimental configurations of each motion step for case 1. (Under tip loads of 2kg weights, -----released rigid limbs, ——locked rigid limbs). (a) The initial state of the manipulator. (b) Step 1 motion using Topology I. (c) Step 2 motion using Topology II. (d) Step 3 motion using Topology I. (e) Step 4 motion using Topology II. (f) When the moving platform of the manipulator reaches the desired pose and all rigid limbs are locked, the shapes of the flexible limbs could be changed by adjusting their extended length.

- The results in Fig. 19 show that the kineto-static model could well simulate the shapes of the manipulator. Besides, when the moving platform of the manipulator reaches the desired pose and all rigid limbs are locked, the flexible limbs could obtain different shapes by adjusting their extended length as shown in Fig. 19(f). This indicates that the proposed manipulator has the ability to adjust the end platform pose and the overall shape independently to some extent. An optimal final shape can be selected for a specific application or an energy-saving shape. This is also a point that we will focus on in future studies.

6. Conclusions

This paper focused on addressing two key issues encountered in the kineto-static analysis of rigid-flexible morphing manipulators. It proposed a framework to establish the kineto-static model and conduct an in-depth analysis of the motion of a 3-DOF morphing manipulator that we have developed.

The first issue involves establishing a coupled relationship for multi-step motion, a crucial aspect for solving the inverse multi-step kinematics problem while incorporating motion planning. The second issue involves investigating the coupled influence between the LVGT and the active PCM. This analysis encompasses various constraints imposed by rigid limbs, the coupled non-linear deformation of flexible limbs, and the different actuation modes of the PCM.

To solve the first problem, we use trajectory constrained equations to describe the coupled relationship for multi-step motion. Model analysis reveals that at least 3 steps are required to maneuver the 3-DOF of the moving platform. Beyond 3 steps, the manipulator can achieve a larger workspace while avoiding singularity poses, but will encounter multiple solutions in IKP. The proposed model can analyze these potential moving paths and select the shortest one as the optimal trajectory.

For the second problem, a kineto-static model is established to analyze actuation distance, actuation forces, and deformed shapes. This model can account for redundant actuation modes through an optimization model, where the optimization goal is to achieve the desired driving force distribution. The model considers constraints from the LVGT, deformation governing equations of flexible limbs (the CBCM model), and static balance equations of the moving platform.

The model demonstrates high accuracy in adjusting the end pose of the manipulator through open-loop position control of the actuator, with an average error of less than 3%. In predicting the actuation forces, the maximum error is less than 15% compared to experimental results. The force error could arise from the dimension error of the prototype, the assumption of not considering the weight of the mechanism itself, and most importantly, the additional force caused by position error in redundant actuated flexible limbs. Therefore, when implementing position control, it is advisable to choose a high-accuracy actuator with a larger actuation force limitation.

The study shows that the redundant actuation modes can significantly change/improve the actuation force distribution. By adjusting the parameters in weight matrix, different actuation force distributions can be obtained. Applying a smaller weight coefficient to the flexible limb with a larger actuation force arm will reduce the actuation forces of the two actuators. Additionally, the influences of the LVGT on the actuation forces and distances are investigated, revealing that a relatively large dimension LVGT with the flexible limb having a larger actuation force arm as the main actuation can help reduce actuation forces.

The proposed model provides a solution for accurately modeling the motion of such a manipulator based on its real motion principle. It can facilitate maneuvering the manipulator to achieve large-scale shape morphing while considering constraints from both rigid and flexible limbs. Additionally, it enables the optimization of actuation force distribution and can be utilized in simulation-based structural optimization of the manipulator. Moreover, the proposed method can serve as a modeling reference for other morphing systems that have rigid constraints and large deformation members.

For future practical engineering applications, when some of the mechanism's motion functions or performance characteristics can be compromised, we can also simplify the design and control strategies based on the configuration studied in this article. For example, when there is a compromise on the manipulators motion functions (such as controllable DOFs and motion precision) or load-bearing performance, appropriate simplifications can be made to the rigid backbones. Besides, if there are no strict design constraints on the magnitude of the driving force or the arrangement of the flexible limbs, simplifications can also be made to the design of the flexible limbs by reducing the number of flexible limbs. In addition, if we can use smart materials and structures to design a flexible limb with sufficient stiffness that can also significantly vary in stiffness, it could perform the dual function of a passive lockable rigid limb and a flexible limb. More specifically, if the stiffness of the flexible limb increases sufficiently, it can be used as a locked rigid limb, and when it becomes soft, it becomes a flexible limb. Using this kind of variable stiffness limb would also reduce the use of rigid lockable limbs, thereby simplifying the structural design and enhance the engineering usability of the manipulator.

Declaration of competing interest

The authors declare no conflict of interest in this paper.

Acknowledgment

This study is sponsored by the National Natural Science Foundation of China (No. 52105002), the Shanghai Pujiang Programme (No. 23PJD069), and the China Scholarship Council (CSC).

Appendix A. Mobility and stability analysis of the manipulator

This appendix gives the method to analyze the mobility and stability of the manipulator in different topologies.

As flexible members with spread compliance are unable to provide strict kinematic constraints, we focus solely on the DOF analysis of the rigid system for the rigid-flexible manipulator proposed in this paper. The mobility of the closed-loop manipulator can be determined using Eq. (A.1) [78], given as

$$M = \lambda(n - g - 1) + \sum_{k=1}^{g} f_k \ , \tag{A.1}$$

where the motion parameter, λ, takes a value of 3 in this planar case. n, g, f_k, and M are the number of links, the number of joints, the degrees of relative motion permitted by joint k, and the DOF of the manipulator, respectively.

When $M > 0$, at least two P joints should be released and the manipulator can be driven by flexible panels. When $M \leq 0$, the manipulator forms a stable truss structure which could be determinate or indeterminate. The degree of static indeterminacy could be examined by the following truss stability equation [79]

$$N = (m + r) - 2v \ , \tag{A.2}$$

where m, v and r are the number of members, joints and unknown reaction components respectively.

Table A.1 gives the parameters and results of the mobility (DOF), as well as the static indeterminacy of the manipulator when the manipulator turns to a truss structure.

Table A.1. Mobility and degree of static indeterminacy of the manipulator

The number of released P joints	Classification	M	N	λ	n	g	f_k	m	v	r
0	Truss structure	–1	1	3	6	8	1	5	4	4
1		0	0	3	7	9	1	4	4	4
2	Rigid-flexible mechanism	1	\	3	8	10	1	\	\	\
3		2	\	3	9	11	1	\	\	\
4	Continuum mechanism	3	\	3	10	12	1	\	\	\

Appendix B. Analytical inverse kinematic solutions for 3-step motions

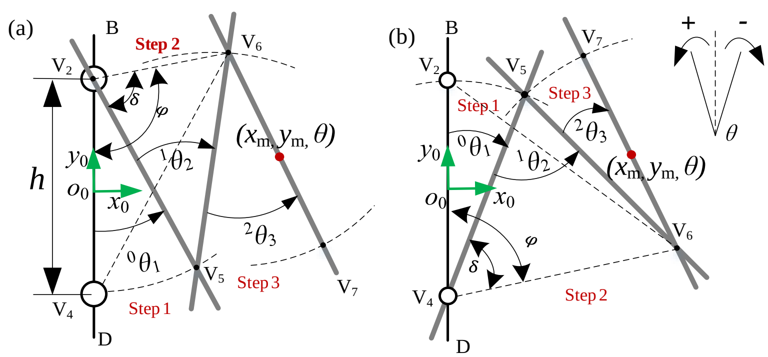

Fig. B.1. Kinematics analysis model for a 3-step motion. (a) gives the analysis model for the moving process of Topology II→ I→ II. (b) gives the analysis model for the moving process of Topology I→II→I.

The analytical inverse kinematic solution for a 3-step motion could be readily obtained by using a geometric method. As shown in Fig. B.1, for a given desired pose of the moving platform (x_m, y_m,θ), the position vectors of V_2, V_4, V_6, V_7 with the {$\boldsymbol{x_0}$, $\boldsymbol{y_0}$} origin could be derived as

$$\begin{cases} \mathbf{V}_2 = \left\{0, \ \dfrac{h}{2}\right\} \\ \mathbf{V}_4 = \left\{0, \ -\dfrac{h}{2}\right\} \\ \mathbf{V}_6 = \left\{x_m - \dfrac{h}{2}\sin\theta, y_m + \dfrac{h}{2}\cos\theta\right\} \\ \mathbf{V}_7 = \left\{x_m + \dfrac{h}{2}\sin\theta, y_m - \dfrac{h}{2}\cos\theta\right\} \end{cases} . \tag{B.1}$$

For the moving process of Topology II→ I→ II (Fig. B.1(a)), using the geometric relationship in $\Delta V_2V_5V_6$, ${}^{1}\theta_2$ could be firstly obtained as

$$^{1}\theta_2 = \arccos\left(\frac{2h^2 - \left\|\mathbf{V_6} - \mathbf{V}_2\right\|^2}{2h^2}\right). \tag{B.2}$$

Then, $^{0}\theta_1$ could be calculated as

$$^{0}\theta_1 = \varphi - \delta \ , \tag{B.3}$$

where δ is the angle between line V_2V_5 and V_2V_6, and φ is the angle between line V_2V_4 and V_2V_6, as labeled in Fig. B.1(b). Using the geometric relationship in $\Delta V_2 V_4 V_6$, δ and φ can be calculated as

$$\begin{aligned} \delta &= \frac{\pi - {}^{1}\theta_2}{2} \\ \varphi &= \arccos\left(\frac{h^2 + \left\|\mathbf{V_2} - \mathbf{V_6}\right\|^2 - \left\|\mathbf{V_6} - \mathbf{V_4}\right\|^2}{2h\left\|\mathbf{V_2} - \mathbf{V_6}\right\|}\right). \end{aligned} \tag{B.4}$$

At last, $^{2}\theta_3$ could be derived as

$$^{2}\theta_3 = \theta - {}^{0}\theta_1 + {}^{1}\theta_2 \ . \tag{B.5}$$

For the moving process of Topology I→II→I shown in Fig. Fig. B.1(b), the inverse kinematic solution could also be obtained using a similar method. Here we directly the results

$$\begin{aligned} {}^{0}\theta_1 &= \varphi - \delta \\ {}^{1}\theta_2 &= \arccos\left(\frac{2h^2 - \left\|\mathbf{V_4} - \mathbf{V_6}\right\|^2}{2h^2}\right) \\ {}^{2}\theta_3 &= -\theta - {}^{0}\theta_1 + {}^{1}\theta_2 \end{aligned} \quad , \tag{B.6}$$

where

$$\begin{aligned} \delta &= \frac{\pi - {}^{1}\theta_2}{2} \\ \varphi &= \arccos\left(\frac{h^2 + \left\|\mathbf{V_4} - \mathbf{V_6}\right\|^2 - \left\|\mathbf{V_5} - \mathbf{V_6}\right\|^2}{2h\left\|\mathbf{V_4} - \mathbf{V_6}\right\|}\right). \end{aligned} \tag{B.7}$$

Appendix C. The Chained Beam-Constraint-Model

This section introduces the deformation governing equations of a large deformation beam used in Sec. 4.1.

(1) Beam-Constraint-Model (BCM)

Figure 10(a) shows a simple beam (length *S*, in-plane thickness *t*, out-of-plane thickness *w*, Young's modulus of the material *E*, the area moment of inertia of the beam cross-section $I=wt^3/12$) subject to transverse force *F*, axial force P and moment M at its free end, resulting in axial and transverse deflections Δ_x and Δ_y, and end slope α. For the plane strain problem in wide beam deformation, $E^* = E/(1-\gamma\text{^}2)$ can be used to modify the Young's modulus, in which γ is Poisson's ratio of the material.

In BCM, the load-deflection relations (corresponding to Eq. (6)) of the beam can be expressed by the following parametric and closed-form equations [71, 73]:

$$\begin{cases} \begin{bmatrix} f \\ m \end{bmatrix} = \begin{bmatrix} g_{11} & g_{12} \\ g_{21} & g_{22} \end{bmatrix} \begin{bmatrix} \delta_{\mathrm{y}} \\ \alpha \end{bmatrix} + p \begin{bmatrix} p_{11} & p_{12} \\ p_{21} & p_{22} \end{bmatrix} \begin{bmatrix} \delta_{\mathrm{y}} \\ \alpha \end{bmatrix} + p^2 \begin{bmatrix} q_{11} & q_{12} \\ q_{21} & q_{22} \end{bmatrix} \begin{bmatrix} \delta_{\mathrm{y}} \\ \alpha \end{bmatrix} \\ \delta_{\mathrm{x}} = \dfrac{t^2 p}{12 S^2} - \dfrac{1}{2} \begin{bmatrix} \delta_{\mathrm{y}} & \alpha \end{bmatrix} \begin{bmatrix} u_{11} & u_{12} \\ u_{21} & u_{22} \end{bmatrix} \begin{bmatrix} \delta_{\mathrm{y}} \\ \alpha \end{bmatrix} - p \begin{bmatrix} \delta_{\mathrm{y}} & \alpha \end{bmatrix} \begin{bmatrix} v_{11} & v_{12} \\ v_{21} & v_{22} \end{bmatrix} \begin{bmatrix} \delta_{\mathrm{y}} \\ \alpha \end{bmatrix} \end{cases} , \tag{C.1}$$

in which all the load parameters and the deflection parameters are normalized with respect to the geometric and material parameters of the beam, given as

$$m = \frac{MS}{EI},\ f = \frac{FS^2}{EI},\ p = \frac{PS^2}{EI}, \delta_{\mathrm{y}} = \frac{\Delta_{\mathrm{y}}(S)}{S}, \delta_{\mathrm{x}} = \frac{\Delta_{\mathrm{x}}(S)}{S}, x = \frac{X}{S}\ , \tag{C.2}$$

and the coefficients *g's*, *p's*, *q's*, *u's* and *v's* of BCM matrices are non-dimensional beam characteristic coefficients given in Tab. C.1.

Table C.1. Beam characteristic coefficients of BCM matrices [73]

g_{11}	$g_{12} = g_{21}$	g_{22}	$p_{11} = u_{11}$	$p_{12} = p_{21} = u_{12} = u_{21}$	$p_{22} = u_{22}$	$q_{11} = v_{11}$	$q_{12} = q_{21} = v_{12} = v_{21}$	$q_{22} = v_{22}$
12	– 6	4	6/5	–1/10	2/15	–1/700	1/1400	–11/6300

To obtain the deflected configuration (shape functions) of the beam, the deflections at any point on the beam are given as follows:

$$\begin{cases} u_x(x) = \dfrac{t^2 x}{12} p - [f \quad m]\begin{bmatrix} c_{11} & c_{12} \\ c_{21} & c_{22} \end{bmatrix}\begin{bmatrix} f \\ m \end{bmatrix} \\ \begin{bmatrix} u_y(x) \\ \theta(x) \end{bmatrix} = \begin{bmatrix} k_{11} & k_{12} \\ k_{21} & k_{22} \end{bmatrix}\begin{bmatrix} f \\ m \end{bmatrix} \end{cases}, \tag{C.3}$$

where $x \in [0,1]$ and the coefficients *k's* and *c's* in the above functions are given in Tab. C.2.

Table C.2. The coefficients *k's* and *c's* in shape functions of BCM [71]

When $P > 0$, $r = \sqrt{p}$	When $P < 0$, $r = -\sqrt{p}$
$k_{11} = \dfrac{\tanh r}{r^3}[\cosh(rx) - 1] - \dfrac{\sinh(rx)}{r^3} + \dfrac{x}{r^2}$	$k_{11} = \dfrac{\sin(r)}{r^3} - \dfrac{x}{r^2} - \dfrac{\tan r}{r^3}(\cos(rx) - 1)$
$k_{12} = \dfrac{\cosh(rx) - 1}{r^2 \cosh r}$	$k_{12} = \dfrac{1 - \cos(rx)}{r^2 \cos r}$
$k_{21} = \dfrac{1 - \cosh(rx) + \tanh r \sinh(rx)}{r^2}$	$k_{21} = \dfrac{\cos(rx) + \tan r \sin(rx) - 1}{r^2}$
$k_{22} = \dfrac{\sinh(rx)}{r \cosh r}$	$k_{22} = \dfrac{\sin(rx)}{r \cos r}$
$c_{11} = \dfrac{\begin{bmatrix} 4rx + 2rx\cosh(2r) - 4\sinh(rx - 2r) - 4\sinh(rx) - \\ \sinh(2r - 2rx) - 3\sinh(2r) \end{bmatrix}}{8r^5 \cosh^2 r}$	$c_{11} = \dfrac{\begin{bmatrix} 4rx + 2rx\cos(2r) - 4\sin(rx - 2r) - 4\sin(rx) - \\ \sin(2r - 2rx) - 3\sinh(2r) \end{bmatrix}}{8r^5 \cos^2 r}$
$c_{12} = c_{21} = \dfrac{\begin{bmatrix} 4\cosh(rx) - 2\cosh^2(rx) + \\ \tanh r(\sinh(2rx) - 2rx) - 2 \end{bmatrix}}{8r^4 \cosh r}$	$c_{12} = c_{21} = \dfrac{\begin{bmatrix} 4\cos(rx) - 2(\cos(rx))^2 - \\ \tan r[\sin(2rx) - 2rx] - 2 \end{bmatrix}}{8r^4 \cos r}$
$c_{22} = \dfrac{\sinh(2rx) - 2rx}{8r^3 \cosh^2 r}$	$c_{22} = \dfrac{2rx - \sin(2rx)}{8r^3 \cos^2 r} n$

(2) The Chained Beam-Constraint-Model

Referring to Figs. 10(b) and (c), the CBCM is composed of multiple BCM [71, 72]. The load equilibrium equations for the first i^{th} (i = 2, · · ; N) element's end loads can be written as (totally 3(N-1) equations)

$$\begin{bmatrix} \cos\theta_i & -\sin\theta_i & 0 \\ \sin\theta_i & \cos\theta_i & 0 \\ (1+\delta_{xi}) & -\delta_{yi} & 1 \end{bmatrix}\begin{bmatrix} f_i \\ p_i \\ m_i \end{bmatrix} = \begin{bmatrix} f_1 \\ p_1 \\ m_{i-1} \end{bmatrix}, \tag{C.4}$$

in which the following relationships hold for the normalized end loads (note that f_1 is parallel to f_0 and p_1 is parallel to p_0) :

$$f_0 = \frac{F_0 S^2}{EI} = N^2 f_1,\;\; p_0 = \frac{P_0 S^2}{EI} = N^2 p_1,\;\; m_0 = \frac{M_0 S}{EI} = N m_N \;. \tag{C.5}$$

Then, the geometric constraint equations of the entire beam can be written as (3 equations)

$$\begin{cases} \sum_{i=1}^{N-1}\left[\begin{bmatrix} \cos\theta_i & -\sin\theta_i \\ \sin\theta_i & \cos\theta_i \end{bmatrix}\begin{bmatrix} S_i(1+\delta_{xi}) \\ L_i\delta_{yi} \end{bmatrix}\right] = \begin{bmatrix} X_0 \\ Y_0 \end{bmatrix}, \\ \theta_N + \alpha_N = \theta_0 \end{cases} \tag{C.6}$$

where S_i is the length of the ith element and $S_i = S/N$ for equal discretization, θ_i is the rotation of the coordinate frame of the i^{th} element with respect to the global coordinate frame, given as $\theta_i = \sum_1^{i-1} \alpha_i$.

Besides, the minimum number of BCM elements (denoted as N_s) required for CBCM to achieve results with satisfactory accuracy can be determined using the following rules of thumb [71]:

$$N_s = \begin{cases} \lceil \max(4\theta_m/\pi), 8Y_{0m}/S \rceil, \text{ no inflection points} \\ \lceil \max(n_i, |2p_m|/\pi) \rceil, \text{ one or more inflection points} \end{cases}, \tag{C.7}$$

where θ_m and Y_{0m} are the maximum values of the tip slope and the vertical tip deflection respectively, n_i represents the number of the inflection points, p_m is the maximum value of the normalized axial force, and $\lceil\cdot\rceil$ denotes the ceiling function.

Appendix D. Derivations for parameters in Jacobian matrix [^{B}**J**]

This section gives the derivations for parameters used in Jacobian matrix [${}^{\mathrm{B}}\mathbf{J}$] introduced in Eq. (9), which include the parameters ${}^{B}\hat{\mathbf{r}}_{\mathrm{P}}$, ${}^{B}\hat{\mathbf{r}}_{F}$, ${}^{\mathrm{B}}\mathbf{L}_{z}\,(z=1,2,3,4)$, σ, β, γ, and ξ.

Referring to Fig. 11, since the fixed end of the flexible panels is perpendicular to the moving platform, { ${}^{B}\hat{\mathbf{r}}_{\mathrm{P}}$ ${}^{B}\hat{\mathbf{r}}_{F}$ } can be written as

$$ {}^{\mathrm{B}}\hat{\mathbf{r}}_{\mathrm{P}} = \{-\cos\theta \;\; \sin\theta\}^{\mathrm{T}},\; {}^{\mathrm{B}}\hat{\mathbf{r}}_{\mathrm{F}} = \{\sin\theta \;\; \cos\theta\}^{\mathrm{T}}. \tag{D.1} $$

In LVGT, ${}^{\mathrm{B}}\mathbf{L}_{z}$ could be calculated as

$$ {}^{\mathrm{B}}\mathbf{L}_{1} = \left\{\frac{\mathbf{L}_{1}}{L_{1}}\right\}^{\mathrm{T}},\; {}^{\mathrm{B}}\mathbf{L}_{2} = \left\{\frac{\mathbf{L}_{2}}{L_{2}}\right\}^{\mathrm{T}},\; {}^{\mathrm{B}}\mathbf{L}_{3} = \left\{\frac{\mathbf{L}_{3}}{L_{3}}\right\}^{\mathrm{T}},\; {}^{\mathrm{B}}\mathbf{L}_{4} = \left\{\frac{\mathbf{L}_{4}}{L_{4}}\right\}^{\mathrm{T}}, \tag{D.2} $$

where $\mathbf{L}_{z}$ and L_{z} could be calculated by using the inverse kinematic model of the LVGT: Given the desired pose (x_{m}, y_{m}, θ) of the moving platform, the position vectors of points V_1, V_2, V_3, V_4, B and D with respect to the origin frame $\{\boldsymbol{x}_{\mathbf{B}}, \boldsymbol{y}_{\mathbf{B}}\}$ can be calculated as

$$ \begin{gathered} \mathbf{V_1} = \left\{0,\;\; \frac{h}{2}\right\}, \mathbf{V_2} = \left\{x_{\mathrm{m}} - \frac{h}{2}\sin\theta, y_{\mathrm{m}} + \frac{h}{2}\cos\theta\right\}, \mathbf{V_3} = \left\{0,\; -\frac{h}{2}\right\}, \mathbf{V_4} = \left\{x_{\mathrm{m}} + \frac{h}{2}\sin\theta, y_{\mathrm{m}} - \frac{h}{2}\cos\theta\right\}, \\ \mathbf{B} = \left\{x_{\mathrm{m}} - \frac{h}{2}\sin\theta, y_{\mathrm{m}} + \frac{h}{2}\cos\theta\right\}, \mathbf{D} = \left\{x_{\mathrm{m}} + \frac{L_{\mathrm{d}}}{2}\sin\theta, y_{\mathrm{m}} - \frac{L_{\mathrm{d}}}{2}\cos\theta\right\}. \end{gathered} \tag{D.3} $$

Then, L_z, σ, β, γ, and ξ could be obtained as

$$ \begin{aligned} &\mathbf{L_1} = \mathbf{V}_1 - \mathbf{V}_2,\; \mathbf{L}_2 = \mathbf{V}_3 - \mathbf{V}_2, \qquad L_1 = \|\mathbf{V}_1 - \mathbf{V}_2\|,\; L_2 = \|\mathbf{V}_3 - \mathbf{V}_2\|, \\ &\mathbf{L}_3 = \mathbf{V}_1 - \mathbf{V}_4,\; \mathbf{L}_4 = \mathbf{V}_3 - \mathbf{V}_4, \qquad L_3 = \|\mathbf{V}_1 - \mathbf{V}_4\|,\; L_4 = \|\mathbf{V}_3 - \mathbf{V}_4\|, \end{aligned} \tag{D.4} $$

$$ \sigma = \arccos\left(\frac{L_1^2 + L_2^2 - h^2}{2L_1L_2}\right),\; \beta = \arccos\left(\frac{L_2^2 + h^2 - L_4^2}{2L_2h}\right),\; \xi = \arccos\left(\frac{L_3^2 + h^2 - L^2}{2L_3h}\right),\; \gamma = \arccos\left(\frac{L_3^2 + L_4^2 - L^2}{2L_3L_4}\right). \tag{D.5} $$

Appendix E. Acronyms used in this paper

LVGT	—	Lockable variable geometry truss
PM	—	Parallel mechanism
PCM	—	Parallel continuum mechanism
FKP	—	Forward kinematics problem
IKP	—	Inverse kinematics problem
BCM	—	Beam constrained model
CBCM	—	Chained beam constrained model
FEA	—	Finite element analysis
MAE	—	Mean absolute error

References

[1] S. Ameduri, A. Concilio, Morphing wings review: aims, challenges, and current open issues of a technology, Proceedings of the Institution of Mechanical Engineers, Part C: Journal of Mechanical Engineering Science, 237 (18) (2020) 0954406220944423.

[2] F. Aimedee, G. Gogu, J.S. Dai, C. Bouzgarrou, N. Bouton, Systematization of morphing in reconfigurable mechanisms, Mechanism and Machine Theory, 96 (2016) 215-224.

[3] Y. Li, Y. Zhao, Y. Chi, Y. Hong, J. Yin, Shape-morphing materials and structures for energy-efficient building envelopes, Materials Today Energy, 22 (2021) 100874.

[4] G. Senatore, P. Duffour, P. Winslow, C. Wise, Shape control and whole-life energy assessment of an ‘infinitely stiff’ prototype adaptive structure, Smart Materials and Structures, 27 (1) (2018) 015022.

[5] L. Korman ková, E. Korman ková, D. Katunský, Shape Design and Analysis of Adaptive Structures, Procedia Engineering, 190 (2017) 7-14.

[6] E. Chang, L.Y. Matloff, A.K. Stowers, D. Lentink, Soft biohybrid morphing wings with feathers underactuated by wrist and finger motion, Science, 5 (38) (2020) eaay1246.

[7] A. Moosavian, F. Xi, S.M. Hashemi, Design and Motion Control of Fully Variable Morphing Wings, Journal of Aircraft, 50 (4) (2013) 1189-1201.

[8] B. Jenett, S. Calisch, D. Cellucci, N. Cramer, N. Gershenfeld, Digital Morphing Wing: Active Wing Shaping Concept Using Composite Lattice-Based Cellular Structures, Soft Robotics, 4 (1) (2016) 33-48.

[9] A. Mukherjee, S.F. Ali, A. Arockiarajan, Compliant structure under follower forces and any combined loading: Theoretical and experimental studies, International Journal of Mechanical Sciences, 153-154 (2019) 75-82.

[10] P. Zhao, J. Liu, C. Wu, Survey on research and development of on-orbit active debris removal methods, Science China Technological Sciences, 63 (11) (2020) 2188-2210.

[11] J. Zheng, R. Li, Z. Xi, Y. Li, The mechanics characteristic of epidermis cell walls in a leaf growth process provides inspiration on a flexible multi-morphing skin, International Journal of Mechanical Sciences, 193 (2021) 106162.

[12] P. Zhao, J. Liu, C. Wu, S. Ye, Q. Yang, G. Hao, Deployment analysis of membranes with creases using a nonlinear torsion spring model, International Journal of Mechanical Sciences, 1 (1) (2023) 108444.
[13] Y. Qin, K. Zhang, J. Li, J.S. Dai, Modelling and analysis of a rigid–compliant parallel mechanism, Robotics and Computer-Integrated Manufacturing, 29 (4) (2013) 33-40.
[14] G. Zhong, B. Peng, W. Dou, Kinematics analysis and trajectory planning of a continuum manipulator, International Journal of Mechanical Sciences, 222 (2022) 107206.
[15] T. Mahl, A. Hildebrandt, O. Sawodny, A Variable Curvature Continuum Kinematics for Kinematic Control of the Bionic Handling Assistant, IEEE Transactions on Robotics, 30 (4) (2014) 935-949.
[16] I.S. Godage, G.A. Medrano-Cerda, D.T. Branson, E. Guglielmino, D.G. Caldwell, Dynamics for variable length multisection continuum arms, International Journal of Robotics Research, 35 (6) (2015) 695-722.
[17] R.J. Webster, B.A. Jones, Design and Kinematic Modeling of Constant Curvature Continuum Robots: A Review, The International Journal of Robotics Research, 29 (13) (2010) 1661-1683.
[18] S. Li, G. Hao, Design and nonlinear spatial analysis of compliant anti-buckling universal joints, International Journal of Mechanical Sciences, 219 (2022).
[19] M. Salerno, K. Zhang, A. Menciassi, J.S. Dai, A Novel 4-DOF Origami Grasper With an SMA-Actuation System for Minimally Invasive Surgery, IEEE Transactions on Robotics, 32 (3) (2016) 484-498.
[20] K. Xu, J. Zhao, M. Fu, Development of the SJTU unfoldable robotic system (SURS) for single port laparoscopy, IEEE/ASME Transactions on Mechatronics, 20 (5) (2015) 2133-2145.
[21] J. Burgner-Kahrs, D.C. Rucker, H. Choset, Continuum Robots for Medical Applications: A Survey, IEEE Transactions on Robotics, 31 (6) (2015) 1261-1280.
[22] B. Balakrisnan, A. Nacev, J.M. Burke, A. Dasgupta, E. Smela, Design of compliant meanders for applications in MEMS, actuators, and flexible electronics, Smart Materials and Structures, 21 (7) (2012) 075033.
[23] A.B. Mackay, D.G. Smith, S.P. Magleby, B.D. Jensen, L.L. Howell, Metrics for Evaluation and Design of Large-Displacement Linear-Motion Compliant Mechanisms, Journal of Mechanical Design, 134 (1) (2012) 011008.
[24] G. Hao, X. Kong, A Novel Large-Range XY Compliant Parallel Manipulator With Enhanced Out-of-Plane Stiffness, Journal of Mechanical Design, 134 (6) (2012) 061009.
[25] A. Parra Rubio, D. Fan, B. Jenett, J. Del Aguila Ferrandis, F. Tourlomousis, A. Abdel-Rahman, D. Preiss, M. Triantafyllou, N. Gershenfeld, Modular Morphing Lattices for Large-Scale Underwater Continuum Robotic Structures, Soft Robotics, 10 (4) (2023) 724-736.
[26] H. Baier, L. Datashvili, Active and morphing aerospace structures-a synthesis between advanced materials, structures and mechanisms, International Journal of Aeronautical Space Sciences, 12 (3) (2011) 225-240.
[27] L.W. Funke, J.P. Schmiedeler, K. Zhao, Design of planar multi-degree-of-freedom morphing mechanisms, Journal of Mechanisms and Robotics, 7 (1) (2015) 011007.
[28] A. Moosavian, C. Zhu Sun, F. Xi, D.J. Inman, Dimensional Synthesis of a MultiLoop Linkage With Single Input Using Parameterized Curves, Journal of Mechanisms and Robotics, 9 (2) (2017) 021007.
[29] P. Shanmugam, S. Raja, K. Parammasivam, F. Zohra, A Study on VGTM Actuation System for Multi Axis Morphing Wing of UAV, 34th AIAA Applied Aerodynamics Conference, Washington, D.C., USA, 2016, 3414-3425.
[30] J.J. Joo, B. Sanders, T. Johnson, M.I. Frecker, Optimal actuator location within a morphing wing scissor mechanism configuration, Smart Structures and Materials 2006: Modeling, Signal Processing, and Control, 2006, 6166: 6124-6135.
[31] I. Dimino, F. Moens, R. Pecora, A. De Gaspari, S. Ricci, S. Ameduri, A. Concilio, U. Mercurio, G.M. Carossa, Morphing Wing Technologies within the Airgreen 2 Project, AIAA Scitech 2022 Forum, 2022, 0718.
[32] L. Campanile, Lightweight Shape-Adaptable Airfoils: A New Challenge for an Old Dream, in: D. Wagg, I. Bond, P. Weaver, M. Friswell (Eds.) Adaptive structures: engineering applications, John Wiley & Sons, UK, 2007, pp. 89-135.
[33] S. Barbarino, O. Bilgen, R.M. Ajaj, M.I. Friswell, D.J. Inman, A Review of Morphing Aircraft, Journal of Intelligent Material Systems and Structures, 22 (9) (2011) 823-877.
[34] H. Tari, G.L. Kinzel, D.A. Mendelsohn, Cartesian and piecewise parametric large deflection solutions of tip point loaded Euler–Bernoulli cantilever beams, International Journal of Mechanical Sciences, 100 (2015) 216-225.
[35] S. Jeong, H.H. Yoo, Flexibility modeling of a beam undergoing large deflection using the assumed mode method, International Journal of Mechanical Sciences, 133 (2017) 611-618.
[36] Y.-J. Kim, S. Cheng, S. Kim, K. Iagnemma, A Stiffness-Adjustable Hyperredundant Manipulator Using a Variable Neutral-Line Mechanism for Minimally Invasive Surgery, IEEE Transactions on Robotics, 30 (2) (2014) 382-395.
[37] C. Yang, S. Geng, I. Walker, D.T. Branson, J. Liu, J.S. Dai, R. Kang, Geometric constraint-based modeling and analysis of a novel continuum robot with Shape Memory Alloy initiated variable stiffness, The International Journal of Robotics Research, 39 (14) (2020) 1620-1634.
[38] A. Bajo, N. Simaan, Hybrid motion/force control of multi-backbone continuum robots, The International Journal of Robotics Research, 35 (4) (2016) 422-434.
[39] M. Mahvash, P.E. Dupont, Stiffness Control of Surgical Continuum Manipulators, IEEE Transactions on Robotics, 27 (2) (2011) 334-345.
[40] X. Luo, D. Song, Z. Zhang, S. Wang, C. Shi, A Novel Distal Hybrid Pneumatic/Cable-Driven Continuum Joint with Variable Stiffness Capacity for Flexible Gastrointestinal Endoscopy, Advanced Intelligent Systems, 5 (6) (2023) 2200403.
[41] X. Duan, W. Yan, G. Chen, H. Wang, Analysis and validation of a planar parallel continuum manipulator with variable Cartesian stiffness, Mechanism and Machine Theory, 177 (2022) 105030.
[42] R.E. Goldman, A. Bajo, N. Simaan, Compliant Motion Control for Multisegment Continuum Robots With Actuation Force Sensing, IEEE Transactions on Robotics, 30 (4) (2014) 890-902.
[43] D. Wei, T. Gao, X. Mo, R. Xi, C. Zhou, Flexible Bio-tensegrity Manipulator with Multi-degree of Freedom and Variable Structure, Chinese Journal of Mechanical Engineering, 33 (1) (2020) 1-11.
[44] Y. Tian, Z. Tian, Y. Zhao, L. Li, F. Xi, Design and Analysis of a Passive Lockable Prismatic Joint for Reconfigurable Mechanisms, The 5th IEEE/IFToMM International Conference on Reconfigurable Mechanisms and Robots (ReMAR 2021), Virtual, online, August 12-14, 2021, 562-571.
[45] Y. Zhao, G. Hao, L. Chai, Y. Tian, F. Xi, A compliant-mechanism-based lockable prismatic joint for high-load morphing structures, Mechanism and Machine Theory, 178 (2022) 105083.
[46] A. Moosavian, M. Rizoiu, F. Xi, Design of a Multifunctional Flow Control Valve for Self-Circulating Hydraulic Cylinders, Journal of Pressure Vessel Technology, 139 (2) (2017) 025001.
[47] F. Aghili, K. Parsa, Design of a Reconfigurable Space Robot with Lockable Telescopic Joints, 2006 IEEE/RSJ International Conference on Intelligent Robots and Systems, Beijing, China, 2006, 4608-4614.
[48] F. Xi, Y. Zhao, J. Wang, W. Wang, Y. Tian, Two Actuation Methods for a Complete Morphing System Composed of a VGTM and a Compliant Parallel Mechanism, Journal of Mechanisms and Robotics, 13 (2) (2021) 021020.
[49] Y. Tian, Y. Zhao, L. Li, G. Yuan, F. Xi, Design and Analysis of a Multi-Segment Shape Morphing Mechanism, Journal of Mechanisms Robotics, 13 (2) (2020) 021004.

[50] Y. Zhao, F. Xi, Y. Tian, W. Wang, L. Li, Design of a planar hyper-redundant lockable mechanism for shape morphing using a centralized actuation method, Mechanism and Machine Theory, 165 (2021) 104439.
[51] J. Wang, J. Yu, L. Zhao, Y. Tian, F. Xi, Y. Zhao, G. Hao, Locking Force and Stiffness Oriented Design for an SMA-Actuated Miniaturized Lockable Prismatic Joint, Under review.
[52] E. Rodriguezleal, J.S. Dai, G.R. Pennock, Inverse Kinematics and Motion Simulation of a 2-DOF Parallel Manipulator with 3-PUP Legs, 5th International Workshop on Computational Kinematics, Essen, Germany, 2009, 85-92.
[53] B. Liao, Y. Lou, Z. Li, Kinematics and optimal design of a novel 3-DoF parallel manipulator for pick-and-place applications, International Journal of Mechatronics and Automation, 3 (3) (2013) 181-190.
[54] M. Husty, I. Birlescu, P. Tucan, C. Vaida, D. Pisla, An algebraic parameterization approach for parallel robots analysis, Mechanism and Machine Theory, 140 (2019) 245-257.
[55] A. Antonov, V. Glazunov, Position, velocity, and workspace analysis of a novel 6-DOF parallel manipulator with "piercing" rods, Mechanism and Machine Theory, 161 (2021) 104300.
[56] Q. Wang, J. Su, Z. Lv, L. Zhang, H. Lin, G. Xu, Efficient hybrid method for forward kinematics analysis of parallel robots based on signal decomposition and reconstruction, Advances in Mechanical Engineering, 9 (5) (2017) 1687814017699094.
[57] H. Shen, D. Chablat, B. Zeng, J. Li, G. Wu, T.-L. Yang, A Translational Three-Degrees-of-Freedom Parallel Mechanism With Partial Motion Decoupling and Analytic Direct Kinematics, Journal of Mechanisms and Robotics, 12 (2) (2020) 021112.
[58] Z. Gong, X. Fang, X. Chen, J. Cheng, Z. Xie, J. Liu, B. Chen, H. Yang, S. Kong, Y. Hao, A soft manipulator for efficient delicate grasping in shallow water: Modeling, control, and real-world experiments, The International Journal of Robotics Research, 40 (1) (2020) 449-469.
[59] C.B. Black, J. Till, D.C. Rucker, Parallel Continuum Robots: Modeling, Analysis, and Actuation-Based Force Sensing, IEEE Transactions on Robotics, 34 (1) (2018) 29-47.
[60] C.E. Bryson, D.C. Rucker, Toward parallel continuum manipulators, IEEE International Conference on Robotics and Automation, 2014, 778-785.
[61] W. Wang, F.F. Xi, Y. Tian, Y. Zhao, Y. Li, Modeling and Analysis of a Planar Soft Panel Continuum Mechanism, Journal of Mechanisms and Robotics, 12 (4) (2020) 044503.
[62] F. Ma, G. Chen, Kinetostatic modeling and characterization of compliant mechanisms containing flexible beams of variable effective length, Mechanism and Machine Theory, 147 (2020) 103770.
[63] T. da Veiga, J.H. Chandler, P. Lloyd, G. Pittiglio, N.J. Wilkinson, A.K. Hoshiar, R.A. Harris, P. Valdastri, Challenges of continuum robots in clinical context: a review, Progress in Biomedical Engineering, 2 (3) (2020) 032003.
[64] D.C. Rucker, B.A. Jones, R.J. Webster III, A Geometrically Exact Model for Externally Loaded Concentric-Tube Continuum Robots, IEEE Transactions on Robotics, 26 (5) (2010) 769-780.
[65] K. Xu, N. Simaan, Analytic Formulation for Kinematics, Statics, and Shape Restoration of Multibackbone Continuum Robots Via Elliptic Integrals, Journal of Mechanisms and Robotics, 2 (1) (2010) 298-320.
[66] J. Till, C.E. Bryson, S. Chung, A. Orekhov, D.C. Rucker, Efficient Computation of Multiple Coupled Cosserat Rod Models for Real-Time Simulation and Control of Parallel Continuum Manipulators, 2015 IEEE International Conference on Robotics and Automation (ICRA), 2015, 5067-5074.
[67] J. Till, D.C. Rucker, Elastic Stability of Cosserat Rods and Parallel Continuum Robots, IEEE Transactions on Robotics, 33 (3) (2017) 718-733.
[68] G. Chen, Z. Zhang, H. Wang, A general approach to the large deflection problems of spatial flexible rods using principal axes decomposition of compliance matrices, Journal of Mechanisms Robotics, 10 (3) (2018) 031012.
[69] G. Chen, Y. Kang, Z. Liang, Z. Zhang, H. Wang, Kinetostatics modeling and analysis of parallel continuum manipulators, Mechanism and Machine Theory, 163 (2021) 104380.
[70] W. Xu, T. Liu, Y. Li, Kinematics, Dynamics, and Control of a Cable-Driven Hyper-Redundant Manipulator, IEEE/ASME Transactions on Mechatronics, 23 (4) (2018) 1693-1704.
[71] F. Ma, G. Chen, Modeling Large Planar Deflections of Flexible Beams in Compliant Mechanisms Using Chained Beam-Constraint-Model, Journal of Mechanisms and Robotics, 8 (2) (2016) 021018.
[72] L.L. Howell, Compliant Mechanisms, Springer, London, 2013.
[73] S. Awtar, S. Sen, A generalized constraint model for two-dimensional beam flexures: nonlinear load-displacement formulation, Journal of Mechanical Design, 132 (8) (2010) 081008
[74] R. L. Williams Ii, J. Pagan, Algae Harvesting from Large Outdoor Ponds Using a Novel Parallel Robot System, Journal of Computer Sciences and Applications, 6 (1) (2018) 38-42.
[75] R.T. Marler, J.S. Arora, The weighted sum method for multi-objective optimization: new insights, Structural multidisciplinary optimization, 41 (1) (2010) 853-862.
[76] P.T. Boggs, J.W. Tolle, Sequential quadratic programming for large-scale nonlinear optimization, Journal of computational applied mathematics, 124 (1) (2000) 123-137.
[77] J. Wang, Y. Zhao, F. Xi, Y. Tian, Design and analysis of a configuration-based lengthwise morphing structure, Mechanism and Machine Theory, 147 (2020) 103767.
[78] K.H. Hunt, Kinematic geometry of mechanisms, The Clarendon Press, New York, 1978.
[79] H. Chi Tran, J. Lee, Force methods for trusses with elastic boundary conditions, International Journal of Mechanical Sciences, 66 (2013) 202-213.